Brain FGF2 and NCAM1 contribute to FGFR1-dependent progression of ER+ breast cancer brain metastases in young and aged hosts

Authors: Morgan S. Fox[1], Jenny A. Jaramillo-Gómez[1], R. Alejandro Marquez-Ortiz[1], Karen L.F. Alvarez-Eraso[1], Maria J. Contreras-Zárate[1], Stella Koliavas[1], Peter Kabos[2,4], Natalie J. Serkova[3,4], Carol A. Sartorius[1,4], Elizabeth A. Wellberg[5], Diana M. Cittelly[*1,4]

Affiliations: [1]Department of Pathology; [2]Department of Medicine, Division of Medical Oncology; [3]Department of Radiology, Animal Imaging Shared Resource; [4]University of Colorado Comprehensive Cancer Center, University of Colorado Denver, Anschutz Medical Campus, Aurora, CO, 80045, USA. [5]Department of Pathology, Harold Hamm Diabetes Center, and Stephenson Cancer Center, University of Oklahoma Health Sciences Center, Oklahoma City, OK, USA.

Contact Information: Diana M. Cittelly Ph.D. 12801 E 17th Ave. University of Colorado Denver, Anschutz Medical Campus, Aurora, CO, 80045. Diana.Cittelly@cuanschutz.edu

Conflict of Interest: MSF, JAJ, RAM, KLFA, MJC, SK, NJS, CAS, EAW, DMC: no conflicts. PK: Clinical research grant support from Genentech, Menarini, Eli Lilly, AstraZeneca.

Authorship contribution: Study supervision: DMC; Conception and design: DMC, MSF, JAJ; Data acquisition, analysis, resources: DMC, MSF, JAJ, RAM, KLFA, MJC, SK, PK, NJS, CAS, EAW. All authors contributed to writing and approved manuscript.

Acknowledgements/Grant Support: This study was supported by DoD-BCRP W81XWH-22-1-0042 (DMC), R37CA227984 (DMC), T32CA190216 (MSF), University of Colorado Cancer Center Pilot Funds (DMC, CAS), the University of Colorado Cancer Center Support Grant (P30CA046934), and NIH High-End and SIFAR S10 Shared Instrumentation Grants (S10OD023485 and S10OD027023). PK is supported by R01CA258766. We would like to thank the Biorepository Core Facility and personnel at the CU Brain Tumor Biorepository for providing de-identified human tissues, the Advanced Light Microscopy Core, Animal Imaging Shared Resource and Jenna Steiner, Genomics Shared Resource and Schuyler Lee, Functional Genomics Shared Resource, Human Immune Monitoring Shared Resource and Kimberly Jordan, and the Cell Technologies Shared Resource for their support of these studies. We would also like to thank Lianne Kraemer, Julia Maués, and Christine Hodgdon for their input and support.

ABSTRACT

Estrogen receptor positive (ER+) breast cancer (BC) represents a significant proportion of BC brain metastasis (BCBM) but remains understudied. Here, we report that FGFR1-amplification, a well-established driver of ER+ BC endocrine resistance, promotes ER+ BCBM colonization in young and aged mice, through brain-dependent mechanisms. FGFR1-dependent brain colonization in young and aged mice occurs via canonical FGF2/FGFR1 signaling and non-canonical NCAM1/FGFR1 interactions. Astrocytic FGF2-mediated paracrine activation of FGFR1 promoted BCBMs in estrogen-treated young mice, but FGF2 signaling decreased in the brain with aging and estrogen-depletion. Neuronal and glial NCAM1, which remain unchanged in young and aged brains, promoted adhesion to neurons and migration of ER+ BC cells, suggesting that interactions with astrocytes and neurons facilitate early ER+ BCBM colonization through FGFR1. Importantly, FDA-approved FGFR inhibitors effectively blocked early but not late metastatic progression only in young mice, suggesting limited efficacy of FGFR inhibitors to block non-kinase-dependent FGFR1 functions *in vivo*.

INTRODUCTION

The management of breast cancer brain metastases (BCBM) has emerged as a critical need for metastatic breast cancer (BC) patients[1]. Once diagnosed, brain metastases (BM) remain incurable, and more than 80% of patients die within one year of their diagnosis[2,3]. While BCBMs show increased incidence in HER2+ and triple-negative (TNBC, lacking estrogen-receptor (ER), progesterone receptor (PR) and HER2) subtypes, up to 16% of patients with metastatic ER+ BC develop BM, and represent a large fraction of patients living with BCBM[4-6].

ER+ BC is effectively treated with anti-estrogen therapies, yet, metastatic ER+ BC commonly arises in older women with tumors refractory to these therapies[5]. ER+ BCBM remains understudied, partly due to the dearth of ER+ mouse models that acquire estrogen (17β-estradiol, E2) independence and express drivers of endocrine resistance observed in humans[7-9]. Although human-derived ER+ transplantable tumors and cell lines (patient-derived xenografts, PDXs) are broadly used to study ER+ BC, their growth in mice requires supplementation with E2 mimicking premenopausal levels, as opposed to more relevant post-menopausal or post-endocrine therapy E2 levels in women[7,8,10-12]. Here, we demonstrate that the aged tumor microenvironment (TME) supports the progression of ER+ BC cells in the absence of E2-supplementation, providing clinically relevant models that mimic the natural progression of metastatic ER+ BC.

Mechanisms of acquired and innate resistance to anti-estrogens in ER+ BC have been the focus of extensive research; yet how specific niches at metastatic sites contribute to endocrine resistance and metastatic recurrence are less understood. FGFR1-amplification was recently reported as the only genomic alteration associated with increased risk of late recurrence in post-menopausal women with ER+ early BC on aromatase inhibitor therapy[13]. Aberrations in FGFR signaling have emerged as critical predictors of metastatic progression in ER+ BC following endocrine therapies[13-18]. A recent study showed that ER+ breast tumors acquire an FGFR4-associated signature that correlated with worse prognosis and provided significant and independent prognostic information for brain, liver, and lung metastasis in ER+ tumors only[15], and suggested that microenvironmental features (either growth factors or specific cell-cell contact) may facilitate growth at metastatic sites. FGFR1 aberrations are significantly higher in BCBM patients compared to non-BM in metastatic BC and predicted poor prognosis[19], further suggesting that FGFR1 may play a specific role in BCBM promotion.

Tyrosine kinase receptor amplification often results in ligand-independent autoactivation; however, FGFR1-amplification alone is insufficient to drive E2-independent growth in models of ER+ BC primary tumors[20]. In the brain, FGFR1 plays known roles in development and is implicated in synaptic repair and maintenance[21-28]. While FGFRs often signal through their cognate FGF ligands, FGFR1 also binds the neural cell adhesion molecule (NCAM), which is expressed on the surface of neurons and glial cells, present at much higher concentrations in the brain than FGFs, and known to activate FGFR1 signaling and regulate synaptic plasticity[21,29-37]. Here, we demonstrate that ER+ FGFR1+ cells have increased ability to colonize the brain in young and aged/E2-suppressed mice, both through canonical FGF2/FGFR1 signaling and non-canonical NCAM1/FGFR1 signaling. While FGF2 promoted strong FGFR1 activation and growth, NCAM1/FGFR1 promoted adhesion to neurons and invasion of ER+ BC cells. Canonical FGF2/FGFR1 signaling decreased in the brain with aging and E2-depletion, and FGFR inhibitors were effective in blocking early but not late metastatic progression, suggesting limited efficacy of FGFR inhibitors to block the spectrum of FGFR1 functions *in vivo*.

RESULTS

ER+ BCBM models recapitulate clinical progression of ER+ BC metastases throughout the lifespan

Analysis of BCBM samples showed that 41/85 (48.2%) originated from ER+ primary BC, with only 14/41 (34.1%) also harboring HER2-amplification (ER+ HER2+), suggesting that the majority of ER+ BCBM are not driven by HER2-amplification (**Fig. 1a**). Patients with ER+ BCBM were primarily postmenopausal at BM diagnosis, either due to age (>50 years) or prior endocrine therapy (**Fig. 1b,c**). Given the lack of ER+ BC models capable of spontaneous brain colonization, we determined the brain-homing ability of ER+ BC cells following hematogenous dissemination. Four ER+ BC PDX-derived cell lines[38] were injected intracardially in young (<12 weeks) female mice, supplemented with E2 to mimic premenopausal human levels[10] and required to drive ER+ BC growth in mice[39]. These cells colonized multiple organs, with brain colonization in 0% (UCD46), 20% (UCD4), 40% (UCD12), and 80% (UCD65) (**Fig. 1d**). Since the majority of ER+ BCBM develops following endocrine therapies, we next determined whether ER+ cells could spontaneously disseminate and outgrow upon endocrine therapy/E2-depletion. For this, we implanted UCD4 or UCD65 cells in the mammary fat pad of young ovariectomized (OVX) female NSG mice supplemented with E2 and allowed tumors to grow until reaching 1 cm^3 to mimic E2-dependent dissemination. Upon tumor removal, mice were randomized into 1) continued E2 supplementation (E2, mimicking E2-dependent metastatic progression in younger women); 2) E2 withdrawal (EWD, mimicking ovarian suppression in younger women); and 3) EWD + letrozole (mimicking full E2-depletion used in post-menopausal women) (**Extended Data Fig. 1a,f**). UCD4 remained E2-dependent for brain and extracranial growth and for dissemination to the brain and other organs (**Extended Data Fig. 1b-e**). BCBMs continued growing in a subset of EWD mice, with macrometastasis incidence of 22.2% in the EWD group and 11% in the EWD+LET group. By contrast, E2 did not promote growth of spontaneously disseminated UCD65 cells in the brain but supported growth extracranially (**Extended Data Fig. 1g,h**). While E2 and EWD+LET-treated mice all showed evidence of disseminated UCD65 cells in the brain, mice succumbed to primary tumor recurrence or extracranial metastases (**Extended Data Fig. 1i,j**). Thus, these models fully recapitulate spontaneous ER+ BC metastasis and provide evidence that ER+ BCBMs emerge under E2-depletion conditions *in vivo.*

Given the low BM outgrowth in spontaneous metastases models which prevents mechanistic studies, we used intracardiac injection, mimicking early events of brain colonization, to determine the BM capability of UCD65 cells in young or aged mice (**Fig. 1e-g**). Consistent with the known E2-dependence of ER+ cells in young mice (<12 weeks), UCD65 cells showed increased incidence (8/13, 62%) and growth in the brain and extracranially in young OVX+ E2 compared to OVX mice (0/14, 0%). However, in aged mice (>52 weeks), BM outgrew in 38% (5/13) and extracranial metastases outgrew in 100% of mice despite low endogenous E2 (**Fig. 1f,g**). BM growth in aged mice was not dependent on low levels of ovarian E2 as UCD65 cells showed similar incidence and progression of BM and extracranial metastases when injected into aged ovariectomized or naïve mice (**Fig. 1h-j**). *Ex vivo* analysis identified GFP+ brain macrometastases (**Fig. 1k**), and MRI analysis of young and aged mice carrying UCD65 BMs confirmed the presence of large intraparenchymal BMs in young and aged mice (**Fig. 1l, Supplemental Fig. 1**). Thus, ER+ BC cells can grow in high E2/young hosts and in low E2/aged hosts.

FGFR1 drives growth of ER+ BC in the brain TME *ex vivo*

As FGFR1-amplification has been reported as the only genomic alteration that predicts increased risk of late metastatic recurrence in anti-estrogen-treated ER+ BC[13]; we interrogated FGFR1 status in ER+ BCBM clinical samples and cells. Immunohistochemistry showed normal or high FGFR1 expression that did not correlate with membrane pFGFR1 status in ER+ BCBM (**Fig. 2a**). ER+ cells with increased brain-colonization ability (UCD12 and UCD65) harbor genomic amplification and increased FGFR1

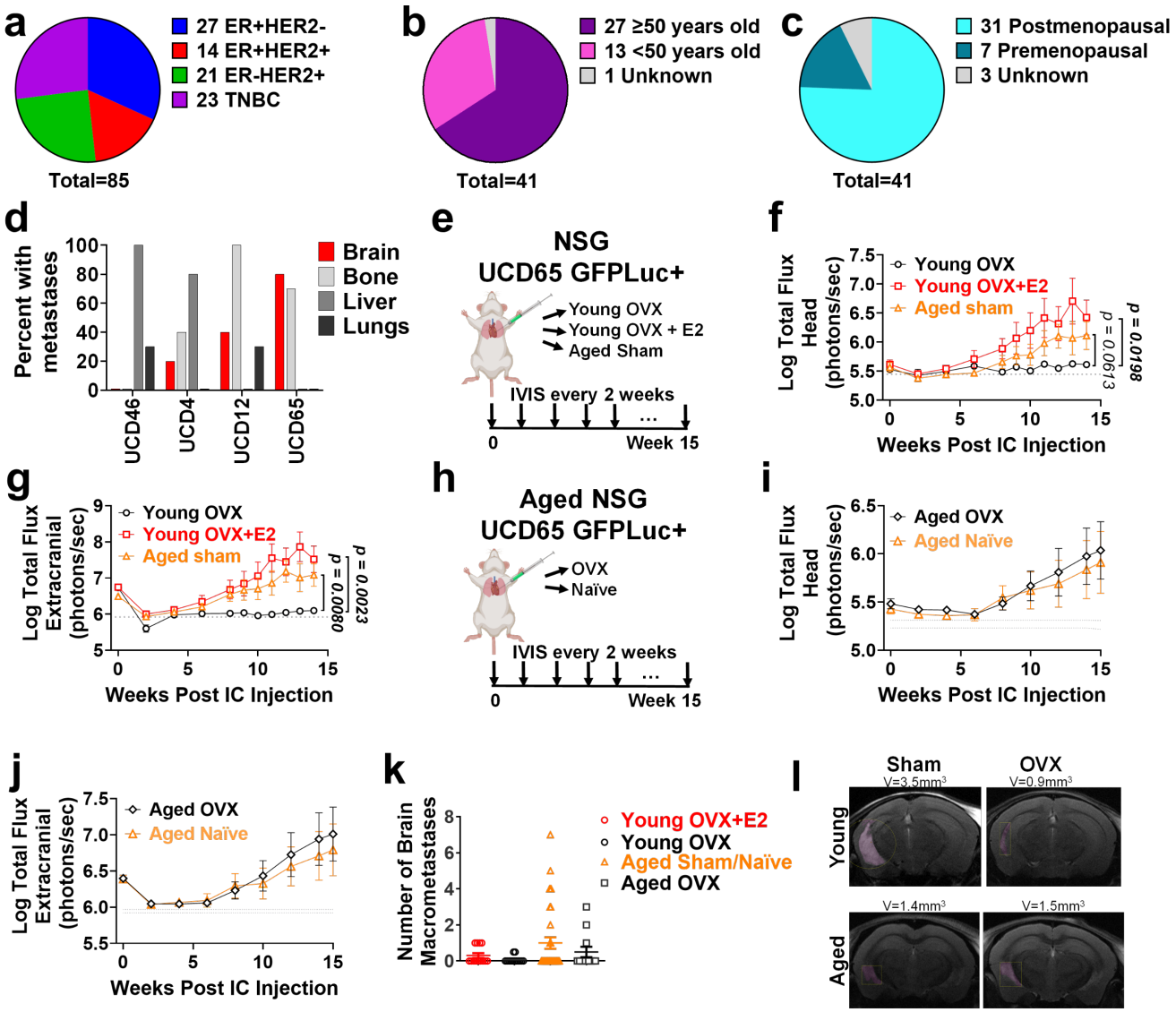

Fig. 1: ER+ PDXs effectively model clinical progression of ER+ BC metastases *in vivo*.
a, A cohort of BCBM from the University of Colorado Cancer Center stratified by primary tumor subtype. **b,** Age distribution of ER+ BCBM patient cohort. **c,** Menopausal status of ER+ BCBM patient cohort. **d,** Frequency of metastasis in brain, bone, liver, and lungs for ER+ PDXs upon intracardiac injection in young mice supplemented with E2 (n=5 per cell line). **e**, UCD65 GFPLuc+ cells were injected intracardially into NSG mice that were i) young OVX (n=14), ii) young OVX+E2 (n=13), or III) aged sham (n=13). **f,** Log-transformed head metastatic burden over time, measured by IVIS. **g,** Log-transformed extracranial metastatic burden over time, measured by IVIS. **h,** UCD65 GFPLuc+ cells were injected intracardially into aged female NSG mice that were i) OVX (n=10) or ii) naïve (n=9). **i,** Log-transformed head metastatic burden over time, measured by IVIS. **j,** Log-transformed extracranial metastatic burden over time, measured by IVIS. **k,** Quantification of number of macrometastases *ex vivo* via stereo-fluorescent microscopy of GFP from all animals shown in **f-j**. **l,** High-resolution fast spin echo T2-MRI (axial planes at 9.4 Tesla) of young (12 weeks) and aged (60 weeks) NSG mice that were OVX or naïve, 16 weeks after UCD65 GFPLuc+ intracarotid artery injection. For **f,g,l,j**, lines denote mean ± SEM. Data were analyzed with 2-way ANOVA or mixed-effects analysis followed by Fisher's LSD test, with p-value shown for last point only. Gray dotted line denotes baseline IVIS signal from tumor-free mouse.

mRNA and protein expression compared to the low and non-brain metastatic UCD4, UCD46, and MCF7 cells (**Fig. 2b,c**). FGFR1 amplification in cell lines was not accompanied by increased autophosphorylation (**Fig. 2c**) or expression of cognate FGFR1-activating ligands (**Supplementary Fig. 2**), suggesting that FGFR1 function may depend on ligand-dependent activation through the TME.

To determine how FGFR1 impacts growth of ER+ BC cells, we stably expressed non-targeting control (shNC) or FGFR1-targeting shRNAs in UCD12 and UCD65 cells (**Fig. 2d, Extended Data Fig. 2**). shFGFR1 and shNC cells showed similar growth in E2-deprived media (vehicle) and in response to E2 in 2D culture (**Fig. 2e,f**). However, when cells were grown as spheroids and plated on organotypic brain slices from young and aged mice, shFGFR1 UCD12 and UCD65 cells showed decreased ability to survive and grow compared to shNC cells (**Fig. 2g-k**). Furthermore, FGFR1-overexpression in MCF7 cells (**Fig. 2l**) did not alter 2D cell growth under E2-deprived or E2-treated conditions compared to empty vector (EV) control cells, but promoted growth in co-culture with organotypic brain slices from young and aged mice (**Fig. 2m-o**). Thus, FGFR1 is a key mediator of survival and growth of ER+ BC cells in the young and aged brain TME.

FGFR1 promotes BCBM colonization of ER+ cells in the young and aged brain TME

To test how FGFR1 impacted brain colonization *in vivo,* we intracardially injected shNC or shFGFR1 UCD65 cells into young ovariectomized mice supplemented with E2 (**Fig. 3a**). FGFR1 knockdown (KD) decreased BCBM progression, but did not affect E2-driven growth of extracranial metastasis (**Fig. 3b-d**). Injection of shNC or shFGFR1 UCD65 in naïve aged mice showed that FGFR1 downregulation decreased BCBM progression and extracranial metastases (**Fig. 3e-h**). Similarly, FGFR1 KD in UCD12 decreased BCBM progression in aged naïve mice and delayed the outgrowth of extracranial metastasis (**Fig. 3i-l**). Moreover, FGFR1-KD cells showed decreased brain signal (but not extracranial signal) within 6 hours post-injection in aged mice (**Fig. 3f,j**), suggesting impaired extravasation into the aged brain parenchyma. Together, these data demonstrate that FGFR1 is a key driver of BCBM progression in the young/E2-high TME and promotes E2-independent brain colonization and extracranial metastases in aged mice.

FGF2/FGFR1 signaling in glial cells decreases upon E2 suppression and aging.

We next interrogated whether host age impacts FGFR1+ ER+ BCBM transcriptional profiles. NanoString GeoMx Digital Spatial Profiling (DSP) followed by UMAP dimension reduction analysis demonstrated no significant differences in the global transcriptional profiles of UCD65 BMs following 6 months of growth in young versus aged sham-mice (**Fig. 4a-d, Supplementary Fig. 3**), suggesting that late-stage ER+ BCBMs are transcriptionally similar, independent of host age. To investigate whether changes in the surrounding brain TME due to aging or ovariectomy may impact FGFR1 function in ER+ BCBMs, GFAP+ and Iba+ glial areas surrounding PanCK+ UCD65 BMs were analyzed using the mouse whole-transcriptome atlas (**Fig. 4e,f**). Dimension reduction analysis using global transcriptomic profiles showed that glial cells surrounding BMs clustered by age and OVX status, with OVX being a major driver of transcriptional changes and inducing aging-related profiles in young mice (**Fig. 4g**). Pairwise comparisons further demonstrated that E2-depletion and aging broadly repressed gene expression (**Fig. 4h**). To visualize the most representative biological patterns, we performed Gene Set Enrichment Analysis (GSEA) and clustered outputs based on shared genes, which identified FGF/FGFR signaling as common top pathways downregulated by OVX and aging (**Fig. 4i-k, Supplementary Table 1**). Fgf2, encoding the canonical FGFR1 ligand, was among the top 20 common downregulated genes with OVX and aging (**Fig. 4h,l,m**), suggesting that paracrine activation of FGFR1 in ER+ BCBMs may be driven by glial FGF2 in young hosts, and decreases with aging and E2-depletion.

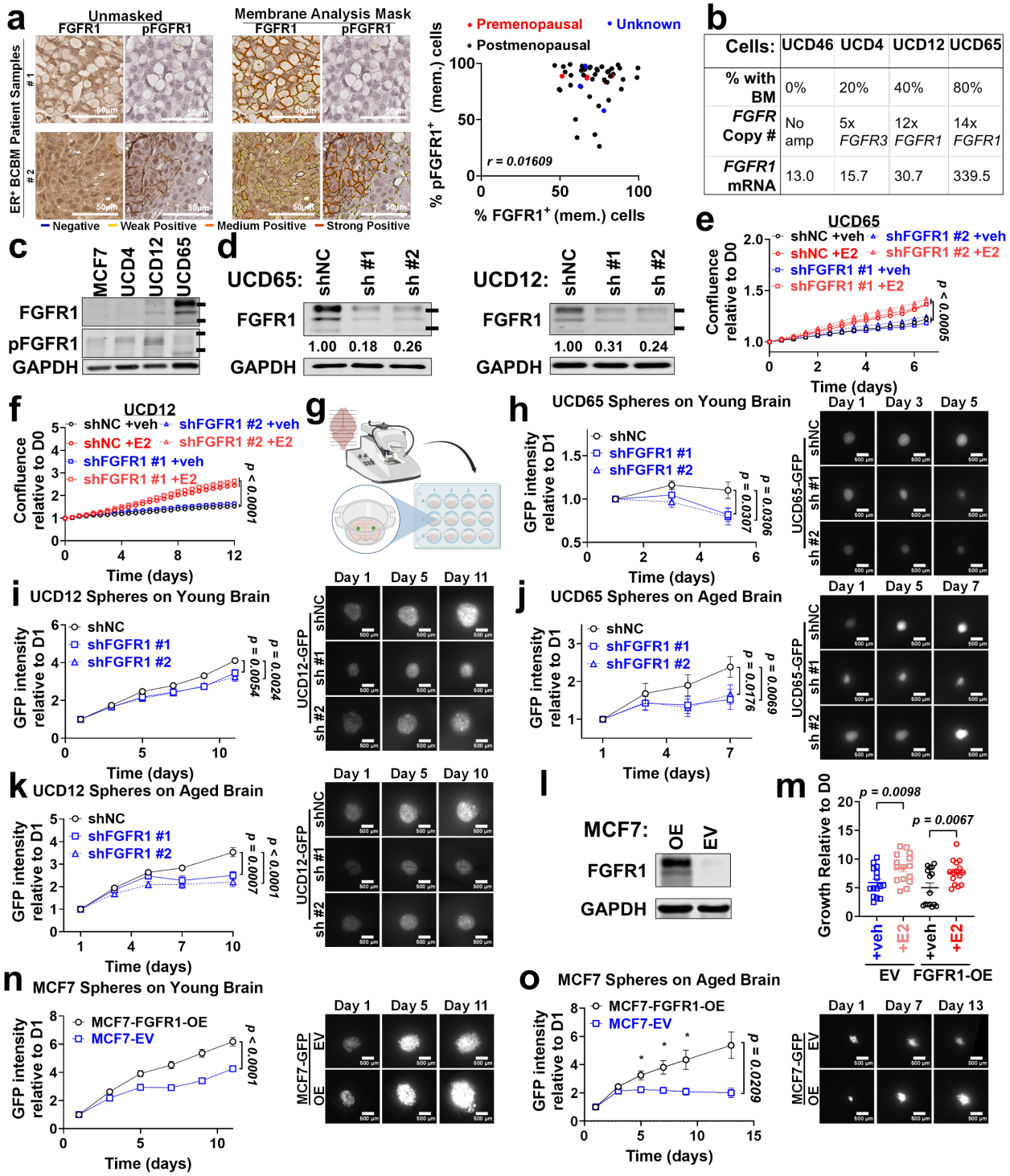

Fig. 2: FGFR1 promotes growth of ER+ BC cells in co-culture systems modeling interactions with the brain microenvironment. **a,** IHC of pFGFR1 and FGFR1 in 48 ER+ BCBM samples (left) and membrane expression mask (right) performed using the Digital Imaging Aperio algorithm for membrane-expression. Right: Spearman correlation of pFGFR1 and FGFR1 membrane expression. **b,** BM frequency, FGFR amplification status, and FGFR1 relative mRNA (FPKM) for ER+ cells. **c,** FGFR1 and pFGFR1 immunoblots in ER+ BC cell lines. **d,** FGFR1 immunoblot in shNC and shFGFR1 UCD65 and UCD12 cells. Numbers indicate relative expression of GAPDH-normalized expression relative to shNC, bars indicate 100kDa and 150kDa. Time course growth of shNC and shFGFR1 UCD65 (**e**) and UCD12 cells (**f**, n=10 replicates per condition) treated with vehicle (EtOH) or 10nM E2. Confluence measured via Incucyte imaging every 12 hours, normalized to time 0. **g,** Schematic of organotypic coculture. UCD65 (**h,** n=12-17) and UCD12 (**i,** n=18-19) spheroid growth on young (9-13w) organotypic brain slices; UCD65 (**j,** n=7-8) and UCD12 (**k,** n=15-16) spheroid growth on aged (49-53w) organotypic brain slices. Graphs show change in GFP intensity per spheroid over time corrected for background fluorescence, normalized to day 1. **l,** FGFR1 immunoblot in MCF7 FGFR1-OE and EV cells. **m,** Fold change growth measured by SRB assay of MCF7 FGFR1-OE and EV cells after 6 days of treatment with 10nM E2 or EtOH vehicle (n=15 replicates per condition). Growth of MCF7 spheroids (n=15-18) on organotypic slices from a young (13w) (**n**) or aged (45w) (**o**) NSG mouse. For **e,f,h-k,n,o**, lines denote mean ± SEM and data were analyzed with 2-way ANOVA followed by Fisher's LSD test. Data in **m** were analyzed by 1-way ANOVA with Fisher's LSD test. All scale bars are 500μm. *:p<0.05

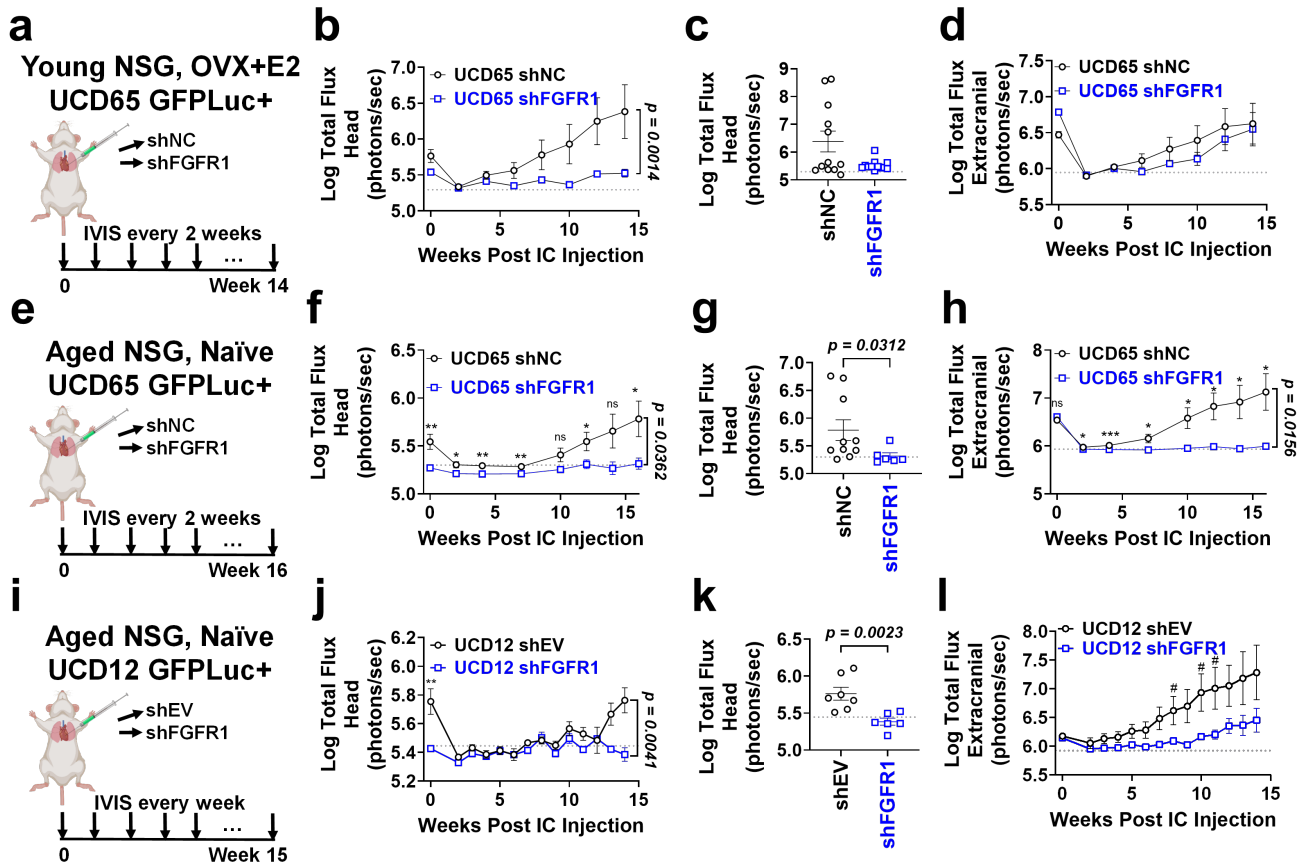

Fig. 3: FGFR1 knockdown decreases ER+ BC brain metastasis in multiple models *in vivo*.
a, shNC (n=12) and shFGFR1 (n=12) UCD65 GFPLuc+ cells were injected intracardially into young (<14w) NSG mice that were OVX+E2. **b,** Log-transformed head metastatic burden over time, measured by IVIS. **c,** Log-tranformed head metastatic burden at endpoint, measured by IVIS. **d,** Log-transformed extracranial metastatic burden over time, measured by IVIS. **e,** shNC (n=10) and shFGFR1 (n=6) UCD65 GFPLuc+ cells were injected intracardially into aged (>52w) naïve NSG mice. **f,** Log-transformed head metastatic burden over time, measured by IVIS. **g,** Log-tranformed head metastatic burden at endpoint, measured by IVIS. **h,** Log-transformed extracranial metastatic burden over time, measured by IVIS. **i,** shEV (n=7) and shFGFR1 (n=6) UCD12 GFPLuc+ cells were injected intracardially into aged (>52w) naïve NSG mice. **j,** Log-transformed head metastatic burden over time, measured by IVIS. **k,** Log-transformed head metastatic burden at endpoint, measured by IVIS. **l,** Log-transformed extracranial metastatic burden over time, measured by IVIS. For **b,d,f,h,j,l,** lines denote mean ± SEM. Data were analyzed with 2-way ANOVA or mixed-effects analysis followed by Fisher's LSD test. P-value shown for last time point only. For **c,g,k**, data were analyzed by Mann-Whitney test. Gray dotted lines denote baseline IVIS signal from a tumor-free mouse. #: p<0.06 *: p<0.05, **: p<0.01, ***:p<0.001.

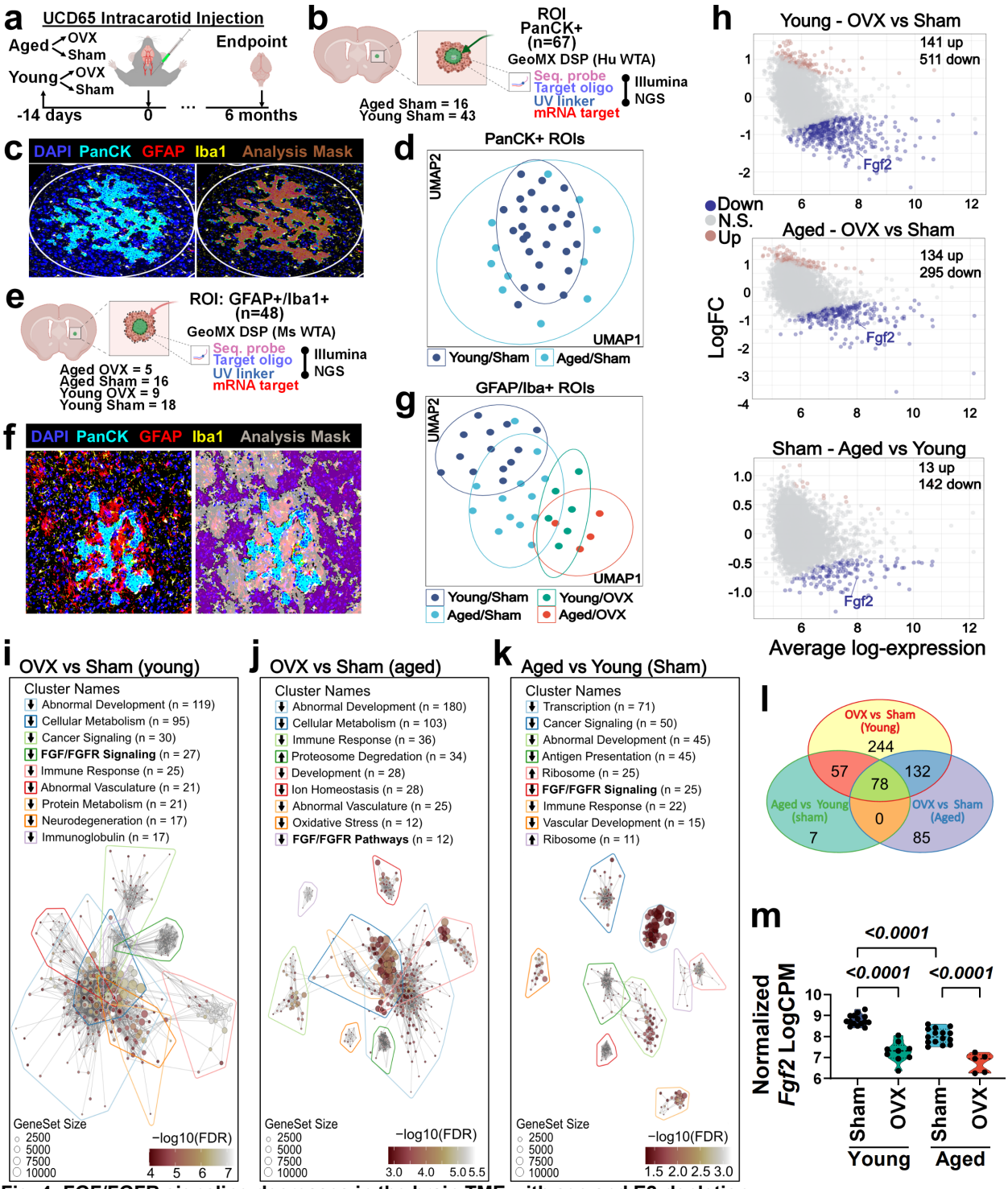

Fig. 4: FGF/FGFR signaling decreases in the brain TME with age and E2-depletion. **a,** Aged (<60w) and young (<15w) NSG mice were OVX or sham operated 14 days before intracarotid-injections of UCD65 cells, and brain metastases allowed to progress for six months. At endpoint animals were perfused and brains harvested and sectioned for GeoMX DSP. **b,** mRNA expression in BMs were measured using human whole transcriptome atlas (WTA) library from NanoString in PanCK+ regions of interest (ROI). **c,** Representative image of stained tissue and PanCK+ mask. **d,** Dimension reduction by UMAP of aged and young sham PanCK+ ROIs. **e,** mRNA expression in glial cells surrounding BMs was measured using mouse WTA NanoString library, using BM-associated GFAP+/Iba1+ ROI. **f,** Representative image of stained tissue and GFAP+/Iba1+ mask. **g,** Dimension reduction by UMAP of GFAP+/Iba1+ ROIs surrounding BM from Young (OVX or sham) and Aged (OVX or sham) mice. **h,** Volcano plots of indicated pairwise comparisons of differentially expressed genes. Significantly differentially upregulated (red) and downregulated (blue) genes are shown. Top 9 differentially expressed clusters of pathways (defined as significant GSEA signatures sharing >35% overlapping genes) for comparisons between young OVX versus sham (**i**), aged OVX versus sham (**j**), and aged versus young sham (**k**) were ordered by number of genesets within the cluster and named based on word frequency in pathway terms. Each node represents a significant geneset, with distance and lines indicating overlap of genes, size representing the number of genes within each geneset, and color representing -logFDR. Repression and enrichment of these gene signatures are indicated with arrows in the legends. **l,** Venn diagram of common downregulated genes in the three indicated pairwise comparisons. **m,** Normalized FGF2 expression within each group (Log(Counts per Million)), analyzed with empirical bayes.

233 **Astrocytes promote FGF2-dependent activation of FGFR1+ ER+ BC cells**

234 We next explored how cells in the brain TME drive canonical FGFR1 activation in young and aged
235 hosts. Consistent with NanoString analysis, FGF2 protein levels were significantly lower in total brain,
236 oligodendrocytes, neurons, and astrocytes from aged versus young mice and in astrocytes aged long-
237 term (>3 months) *in vitro* (**Fig. 5a-c**). Since astrocytes expressed the highest FGF2 levels in the brain,
238 we first tested how astrocytic FGF2 impacted FGFR1-dependent ER+ BC growth. Stimulation of
239 UCD65 cells with conditioned media (CM) from young astrocytes activated FGFR1 and downstream
240 Akt and ERK signaling, which was partially blocked with the FGFR-targeting inhibitor Ponatinib (**Fig.**
241 **5d**). CM from young astrocytes promoted UCD65 growth to levels comparable to FGF2, and this was
242 partially blocked with Ponatinib (**Fig. 5e**). Co-culture with young human primary astrocytes promoted
243 UCD12 and UCD65 cell growth, and was sensitive to FGFR1 downregulation (**Extended Data Fig.**
244 **3a,b**), further suggesting that astrocytic-dependent growth of ER+BC cells is in part mediated by
245 FGF2/FGFR1 signaling. UCD65 cells showed increased pFGFR1 when co-cultured with young and
246 aged astrocytes in E2-free media, but activation was higher with young astrocytes (**Fig. 5f**). E2-
247 independent growth of UCD65 cells was higher in co-culture with young astrocytes than with aged
248 astrocytes, and FGFR1 KD significantly decreased growth in co-culture with both young and aged
249 astrocytes (**Fig. 5g,h**). Thus, age-induced changes in astrocytic FGF2 levels correlate with increased
250 FGFR1 activation and growth in ER+ BC, which diminishes with astrocyte age. Astrocytic age did not
251 differentially impact mammosphere-initiating ability of shEV or shFGFR1 UCD65 cells, but FGFR1
252 downregulation decreased this effect (**Fig. 5i, Extended Data Fig. 3c,d**). Together, these results
253 suggest that FGFR1 is critical for tumor initiation and outgrowth in the absence of exogenous E2, and
254 that young but not aged astrocytes can support E2-independent proliferation of FGFR1+ BC cells.

255 **NCAM1 activates FGFR1 in ER+ BC**

256 Given that brain FGF2 levels decrease with age and E2-suppression, and aged astrocytes were less
257 effective in promoting FGFR1-dependent growth, we investigated whether non-canonical mechanisms
258 of FGFR1 function could impact ER+ BCBM in the absence of high FGF2. NCAM1 is a cell adhesion
259 molecule expressed in neurons and astrocytes (**Extended Data Fig. 4a**) known to activate FGFR1 and
260 important for neural development and synaptic plasticity[31,37,40-42]. To determine if NCAM1 could activate
261 FGFR1 kinase signaling in ER+ BC cells, we treated UCD65 cells with NCAM1 and found dose-
262 dependent activation of FGFR1, Akt, and ERK (**Fig. 6a**), even at the lowest dose (which is below
263 reported NCAM1 cell surfaces levels in the brain[31,32]). NCAM1-induced signaling is dependent on
264 FGFR1 overexpression, as it was only observed in MCF7-FGFR1-OE but not MCF7-EV cells (**Fig. 6b**).
265 The ATP-competitive FGFR kinase inhibitor BGJ398 (Infigratinib) blocked FGF2 and NCAM1-induced
266 FGFR1 signaling in UCD65, UCD12, and MCF7-FGFR1-OE at multiple time points (**Fig. 6c, Extended**
267 **Data Fig. 4b**). Since NCAM1 is mostly membrane-anchored, we next tested whether surface NCAM1
268 from neighboring cells activates FGFR1 by co-culturing ER+ BC cells with NCAM1+ SY5Y
269 neuroblastoma cells stably expressing shEV or shNCAM1 (**Fig. 6d, Extended Data Fig. 4c**). All ER+
270 FGFR1+ cells showed decreased FGFR1 phosphorylation when co-cultured with shNCAM1 versus
271 shEV SY5Y (**Fig. 6e,f**). Thus, these results indicate that neuronal and astrocytic NCAM1 can activate
272 FGFR1 in ER+ BC cells upon arrival to the brain niche.

273 **NCAM1/FGFR1 communication drives interactions between ER+ BC and neurons**

274 We next investigated the physiological effects of NCAM1-mediated FGFR1 activation in ER+ BC cells.
275 While E2 and FGF2 increased UCD12 and UCD65 proliferation, exogenous NCAM1 stimulation (at a
276 dose limited by solubility *in vitro*) did not, despite activating kinase signaling (**Fig. 7a**)**.** To define
277 downstream mechanisms resulting from NCAM1or FGF2-mediated FGFR1 activation, we performed
278 global gene expression profiling of UCD12 and UCD65 cells treated with vehicle, NCAM1, or FGF2 for

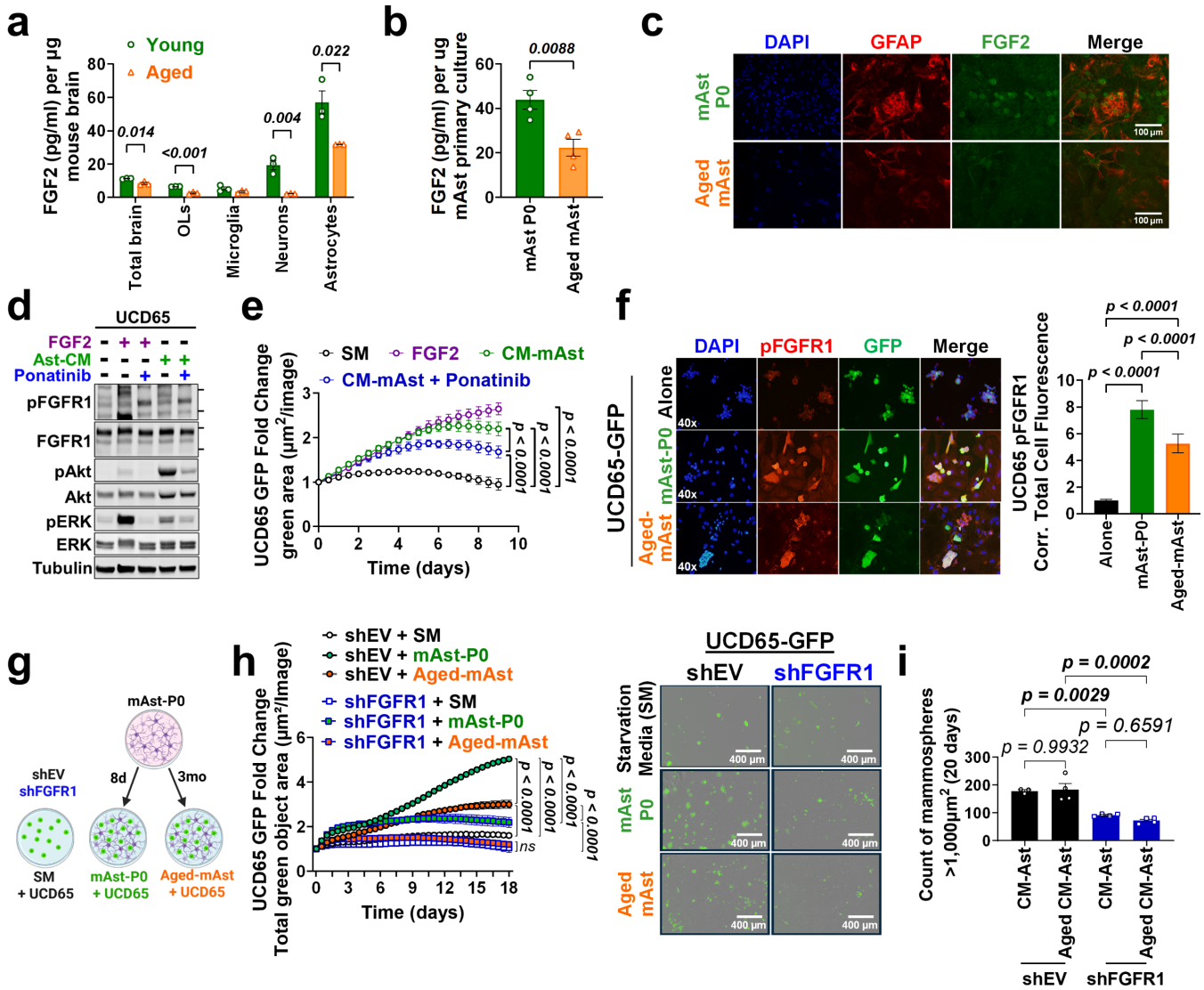

Fig. 5: Astrocytes promote canonical FGF2-dependent activation of FGFR1 in ER+ BC

a, FGF2 ELISA from total brain, oligodendrocyte (OL), microglia, neuron, and astrocyte lysates isolated from young (12 weeks) and aged (>56 weeks) female mice (n=3). **b,** FGF2 ELISA from young (mAst P0, 15 days *in vitro*) and aged (Aged mAst, 90 days *in vitro*) mouse primary astrocyte lysates (n=4). **c,** Immunofluorescence of GFAP and FGF2 in mAst-P0 and aged-mAst. **d,** Immunoblot of UCD65 cells starved for 72 hours, pre-treated with vehicle or Ponatinib (1 µM, 1 hour), followed by FGF2 (10 ng/ml) or 10X astrocyte-conditioned media (CM-Ast) for 10min. **e,** UCD65-GFP+ cells (n=6 replicates per condition) treated with starvation media (SM), CM-mAst, FGF2 (10ng/ml) or CM-mAst + Ponatininb (1 µM). Graphs show fold change in total green area relative to time 0, measured by Incucyte. **f,** Immunofluorescence of pFGFR1 in UCD65 alone or co-cultured with mAst-P0 and aged-mAst. Right: pFGFR1 Corrected Total Cell Fluorescence in UCD65 (n=228-303 cells per group). **g,** Schematic of co-cultures of UCD65 shEV and shFGFR1 cells with mAst-P0 or aged-mAst. **h,** Fold change in total green area relative to time 0 of UCD65 shEV and shFGFR1 cells cultured alone or with mAst-P0 or Aged-mAst (n=3 replicates per condition), measured by Incucyte. Right: Representative images at 18 days. **i,** Number of mammospheres with area >1,000 µm² across four 96-well plates per cell (UCD65 shEV or UCD65 shFGFR1), treated with CM-mAst or Aged-CM-mAst. Number and area were quantified using Incucyte and ImageJ. For **a,b,I,** data were analyzed with 1-way ANOVA followed by Fisher's LSD test. **f** was analyzed with Kruskal-Wallis test followed by Dunn's multiple comparison test. Adjusted P-value shown. For **e,h,** line denotes mean ±SEM, data were analyzed with 2-way ANOVA followed by Fisher's LSD test. P-values shown for last time point only.

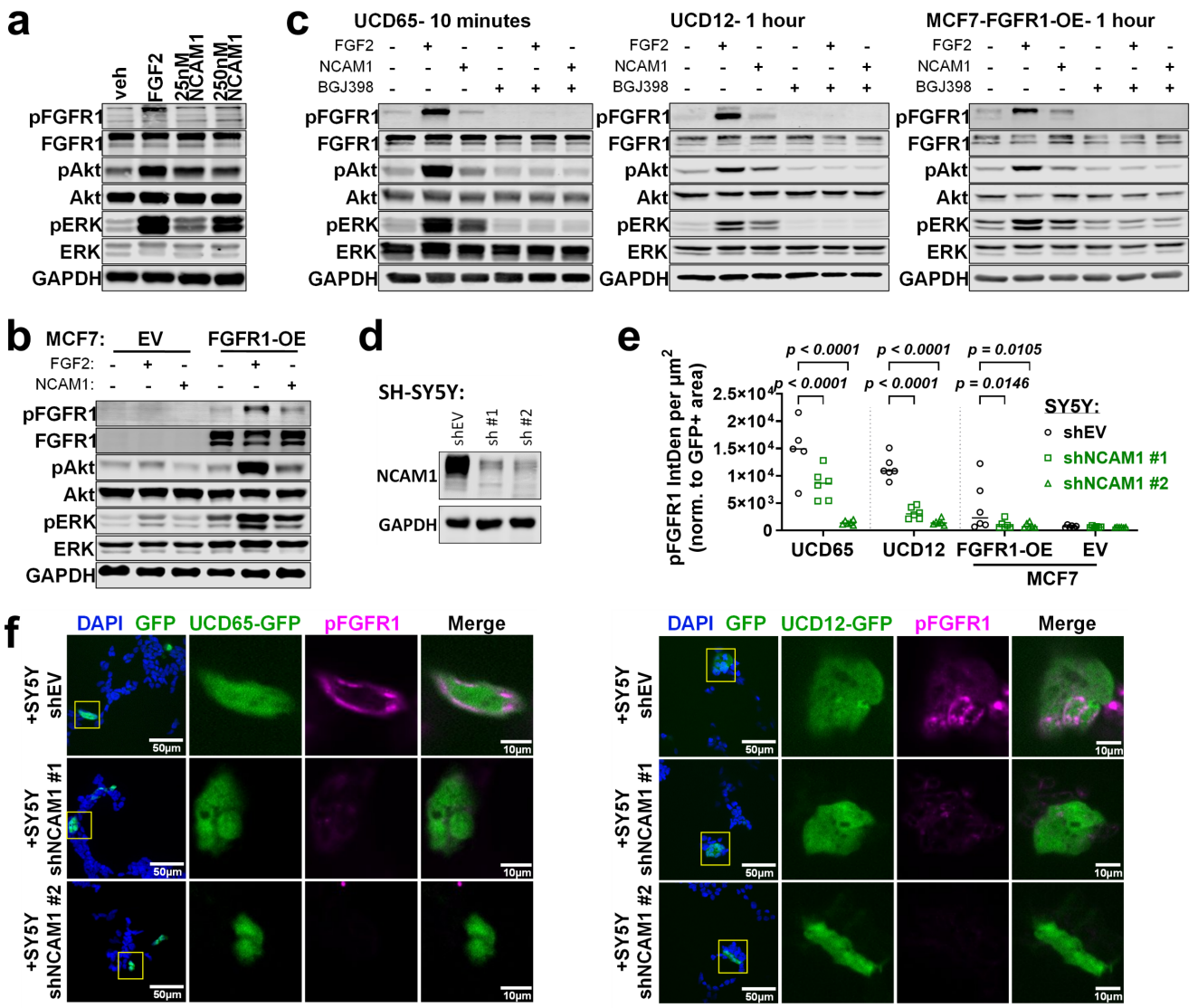

Fig. 6: NCAM1 activates FGFR1 in ER+ BC

a, UCD65 cells were serum-starved and then treated with FGF2 (10ng/mL), 25nM or 250nM recombinant human NCAM1, or vehicle for 10 minutes. Immunoblot shows pFGFR1, FGFR1, pAkt, Akt, pErk, ERK. GAPDH is loading control. **b,** Immunoblot from MCF7 EV and FGFR1-OE cells treated with 10ng/mL FGF2, 250nM NCAM1, or vehicle for 1 hour. **c**, Immunoblot from UCD65, UCD12, and MCF7 FGFR1-OE cells pretreated with 10µM BGJ398 or vehicle for 1 hour, then treated with 10ng/mL FGF2, 250nM NCAM1, or vehicle for the indicated times. **d,** Immunoblot for NCAM1 in SH-SY5Y cells expressing shEV or shNCAM1. **e,** pFGFR1 immunostaining in UCD65, UCD12, MCF7-FGFR1-OE, and MCF7-EV cells cultured on top of shEV or shNCAM1 SH-SY5Y cells (n=5 replicates per condition). Graph shows pFGFR1 Intensity in GFP+ areas, analyzed by 1-way ANOVA followed by Fisher's LSD test. **f,** Representative images of UCD65 cells (left) and UCD12 cells (right) co-cultured with shEV and shNCAM1 SH-SY5Y cells.

24h (**Fig. 7b, Extended Data Fig. 5a-c**). GSEA identified gene signatures shared by both cell lines that were commonly enriched or repressed by NCAM1 and FGF2 or uniquely regulated by each ligand (**Fig. 7c, Supplementary Table 3**). FGF2 and NCAM1 commonly induced 1,390 gene signatures, primarily clustered as signaling associated with development and disease, DNA replication, and immunity. FGF2 induced 2,879 unique differential signatures, demonstrating enrichment of canonical growth factor receptor signaling, cytoskeleton organization, ECM interactions, and transmembrane transport and secretion (**Extended Data Fig. 5d,e; Supplementary Tables 4,5**). By contrast, NCAM1 treatment induced 90 unique differential gene signatures, primarily classified by disease and cell signaling activation, metabolic changes, transmembrane transport, and, interestingly, neuronal gene signatures (**Fig. 7d; Extended Data Fig. 5f,g**). These neural signatures showed enrichment in differentiation, development, and adhesion, with repression of postsynaptic membrane protein localization and trafficking, and myelination/ensheathment (**Fig. 7e**). Therefore, these results suggest that FGF2 promotes broad transcriptional changes, driving canonical signaling through FGFR1 and proliferation, while NCAM1 may drive specific gene signatures promoting neural interactions in ER+ BC cells.

Given the known roles of NCAM/FGFR1 interactions in modulating synaptic plasticity, the induction of synaptic-related gene signatures upon NCAM1 treatment in UCD65 and UCD12 cells, and emerging evidence that direct and indirect synaptic communication between neurons and disseminated brain metastatic cells are key mediators of BCBM outgrowth[43-45], we next determined how FGFR1 impacts cancer-neuron interactions. FGFR1 KD resulted in decreased density of excitatory synapses at the interface of UCD65 spheroids and organotypic brain slices, suggesting that FGFR1 contributes to synaptic localization or interaction between ER+ BC cells and organotypic brain slices (**Fig. 7f**). Furthermore, coculture with primary hippocampal neurons from postnatal mice demonstrated that ER+ BC cells bind and migrate along neurites *in vitro*, and FGFR1 KD significantly decreased the distance migrated by UCD65 and UCD12 cells along these neurites (**Fig. 7g,h**). NCAM1 KD in SY5Y cells decreased migration of UCD65 and UCD12 cells in co-culture (**Fig. 7i**). Together, these results suggest that FGFR1 promotes neuronal interactions and that FGFR1/NCAM1 facilitates migration of ER+ BC cells.

FGFR1 kinase inhibition is effective only in early-stage BCBMs with high FGFR1 activation.

While glial FGF2 decreased with aging and E2-suppression, NCAM1 is highly expressed in the brain TME[31,32], with similar levels in aged and young mice (**Extended Data Fig. 4d-f**). Thus, FGF2 and NCAM1 interactions likely drive FGFR1 activation in ER+ BCBMs in young and aged hosts. Surprisingly, late-stage UCD65 BCBMs from young and aged mice showed minimal membrane pFGFR1 (**Fig. 8a**), which was consistent with the lack of correlation between pFGFR1 status and total FGFR1 expression observed in clinical samples (**Fig. 2a**) and suggested that FGFR1 levels do not fully predict its function, activation, or dependency in established BCBMs. Since interactions with astrocytes and neurons occur from early stages of metastatic colonization, we assessed UCD65 FGFR1 activation 5 days following intracardiac injection in young and aged hosts. Membrane pFGFR1 expression was found in 83% of early disseminated cells in young mice and 57% in aged mice, and membrane pFGFR1 intensity was stronger in disseminated cells in young compared to aged brains (**Fig. 8b,c**), suggesting that transient TME-mediated FGFR1 activation is critical for early brain colonization, particularly in the young brain with high FGF2 expression, but may be dispensable at late stages of BM progression. To test this, we injected UCD65 cells in young mice supplemented with E2 or in aged naïve mice (**Fig. 8d,g**) and began treatment with vehicle or BJG398 either immediately after injection or upon detectable brain metastatic outgrowth. In young mice, FGFR inhibition significantly reduced brain colonization and BCBM outgrowth when started at the time of cell injection but showed no benefit when started at week 7 (**Fig. 8e,f**). However, the inhibitor did not alter E2-dependent extracranial growth (**Extended Data Fig. 6a**). By contrast, FGFR inhibition did not impact BM colonization or extracranial

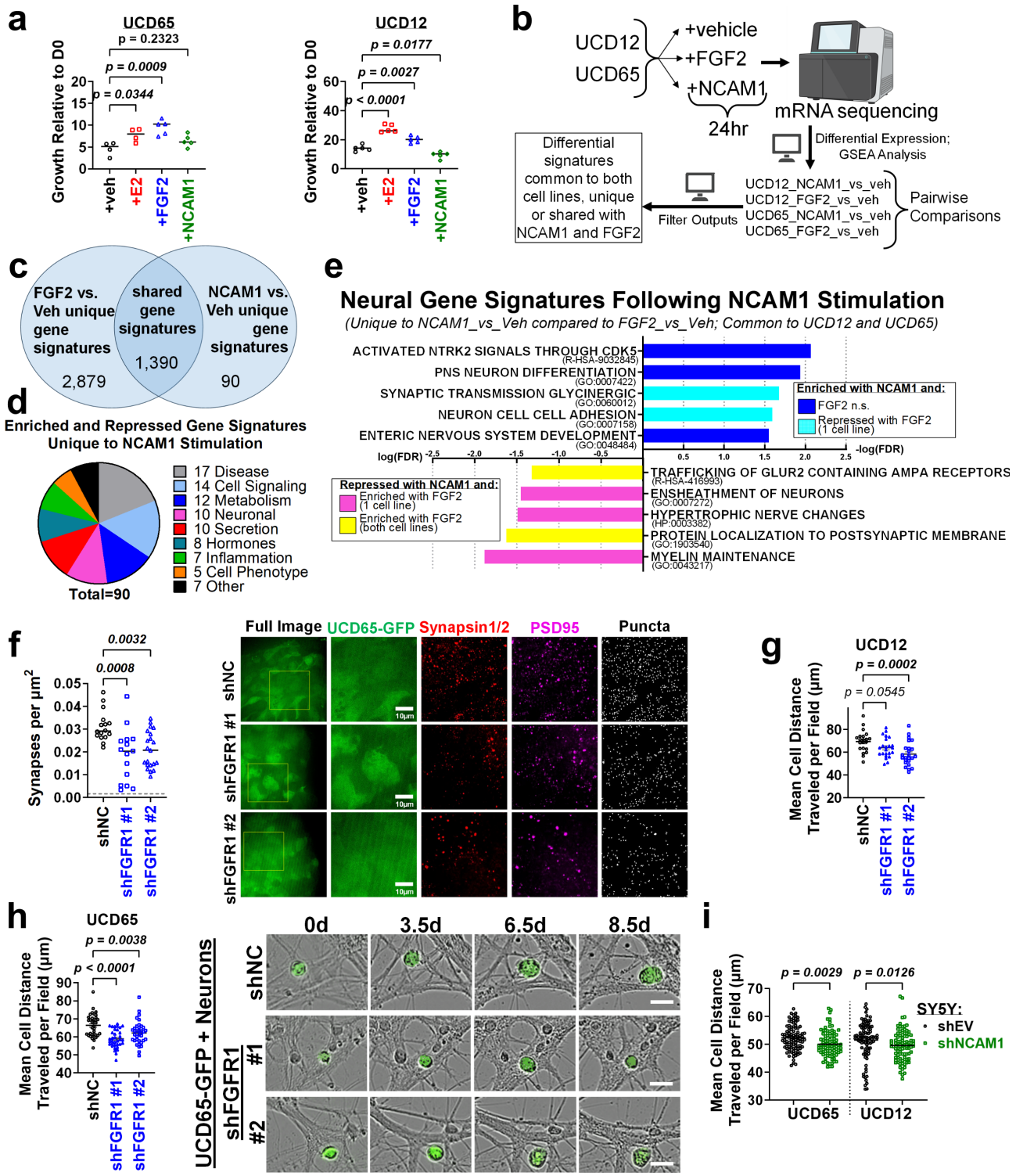

Fig. 7: NCAM1/FGFR1 drives interactions between ER+ BC and neurons

a, Fold change growth (SRB assay) of UCD65 and UCD12 cells with vehicle, 10nM E2, 10ng/mL FGF2, or 250nM NCAM1 for two weeks. (n=4-5). **b,** RNA-sequencing schematic for UCD12 and UCD65 cells treated with vehicle, 10ng/mL FGF2, or 20ug/mL NCAM1 for 24hr (n=3). **c,** Venn diagram shows unique and shared significant gene signatures following FGF2 and NCAM1 treatment. **d,** Pie chart of gene signature categories differentially induced by NCAM1 treatment. **e,** log(FDR) of significant neural gene signatures differentially enriched or repressed following NCAM1 treatment. **f,** Immunofluorescent staining of PSD95 and Synapsin1/2 in shNC and shFGFR1 UCD65 spheroids in co-culture with organotypic brain slices from aged NSG female mice (>59w) for 3 days. Punctate colocalization (n=15-21 images) was quantified. 5,000 GFP+ shNC and shFGFR1 UCD12 (**g**) or UCD65 (**h**) cells were plated on coverslips with 315,000 primary hippocampal neurons (DIV: 8) and imaged every 12 hours for 6-9 days via Incucyte. Cell migration was measured and mean distance per cell within each image (n=24-36) was plotted. Right: representative images of UCD65 cells. Scale bars: 20µm. **i**, 5,000 UCD12 and UCD65 cells were plated on a monolayer of shEV or shNCAM1 SY5Y cells and imaged every 12 hours for 6.5 days via Incucyte. Cell migration over time was measured and mean distance per cell within each image (n=96) was plotted. For **a,f,g,h,i**, data were analyzed by 1-way ANOVA followed by Fisher's LSD test.

progression in aged naïve mice (**Fig. 8h,i; Extended Data Fig. 6b**), suggesting that lower pFGFR1 in the aged TME and at later stages of BM progression result in decreased sensitivity of ER+ BCBM to this FGFR1 kinase inhibitor despite FGFR1-amplification.

Together, our data suggests a model whereby FGFR1 activation in disseminated FGFR1-amplified ER+ BC cells drives neural/astrocytic interaction and migration through NCAM1 and proliferation through FGF2, resulting in FGFR1-dependent early colonization. High levels of FGF2/FGFR1 activation in young hosts are more susceptible to FGFR inhibition compared to the lower FGFR1 activation in aged hosts. Late-stage BCBMs are no longer dependent on these interactions and are not effectively targeted by FGFR inhibitors (**Fig. 8j**).

DISCUSSION

FGFR1-amplification has been shown to promote endocrine resistance in ER+ primary BC by maintaining ligand-independent ER transcription[16,17], yet how the TME influences endocrine resistance at metastatic sites is less understood. Here we demonstrate that the increased BM potential of FGFR1+ ER+ BC cells results from interactions with canonical and non-canonical FGFR1 activation through astrocytes and neurons during early stages of BM colonization. Moreover, our data demonstrates that TME-mediated activation of FGFR1 in ER+ BCBMs is critical for early but not late stages of BM colonization, which has profound implications for the use of FGFR inhibitors clinically.

Our results are in alignment with prior work showing that microenvironment-dependent activation of FGFR1 drives FGFR1-mediated ER signaling and endocrine therapy resistance in primary tumors[14]. FGFR ligands secreted by adipose tissue support ER+ primary tumor growth in obese post-menopausal mouse models[20], and cells within the bone TME secrete FGF2 to promote ER+ BC cell plasticity[46]. However, our studies further demonstrate that the levels of FGFR1-activating ligands in the TME are key determinants of the dependency of ER+ BC cells for FGFR1 activation and response to FGFR inhibition.

Consistent with findings in rats[47,48], our studies show for the first time that E2-suppression and aging downregulate FGF2 levels in the brain niche and directly impact FGFR1 activation. We showed the novel finding that NCAM/FGFR1 interactions lead to FGFR1 kinase signaling activation and promote invasive and migratory phenotypes in ER+ BC cells. While FGF2 decreases with aging and E2-depletion, NCAM1 expression remained unchanged, suggesting that FGFR1/NCAM interactions contribute to FGFR1 function throughout the progression of ER+ BCBMs. Since the affinity of FGF for FGFR is approximately 10^6 times higher than that of NCAM1 for FGFR[31,32], is likely that higher FGF2 levels drive FGFR1 activation and function in young females. By contrast, NCAM1, which is constantly present cell surfaces at a much higher concentration (micromolar) than FGFs, may be a more potent driver in the aged/E2-depleted brain TME[30-32,40,49]. We recognize that our studies cannot fully address the individual contribution of brain FGF2 versus NCAM1 to FGFR1 function in young versus aged females, yet these findings align with studies in HeLa cells showing that despite similar kinase signaling activation, FGF2/FGFR1 signaling promotes proliferation while NCAM1/FGFR1 signaling induces cell migration but not proliferation[41,50]. The extent to which FGF2 and NCAM induce differential levels of pFGFR1 or trigger different recycling of FGFR from the cell membrane may underly how susceptible this activation is to kinase inhibitors[41].

Seminal studies demonstrated that brain metastatic growth of cancer cells depends on their ability to form synapses with neurons[44,45], similar to findings in glioma cells[51,52]. Additional studies suggest that formation of synaptic structures involving presynaptic neurons, astrocytes, and tumor cells is a critical adaptation for BM colonization[43]. Our data showing that FGFR1 promotes increased synaptic puncta with neurons is suggestive of cancer-neuron synapse formation. While definitive proof that these interactions result in synaptic communication in ER+ BC cells is warranted, the formation of synaptic

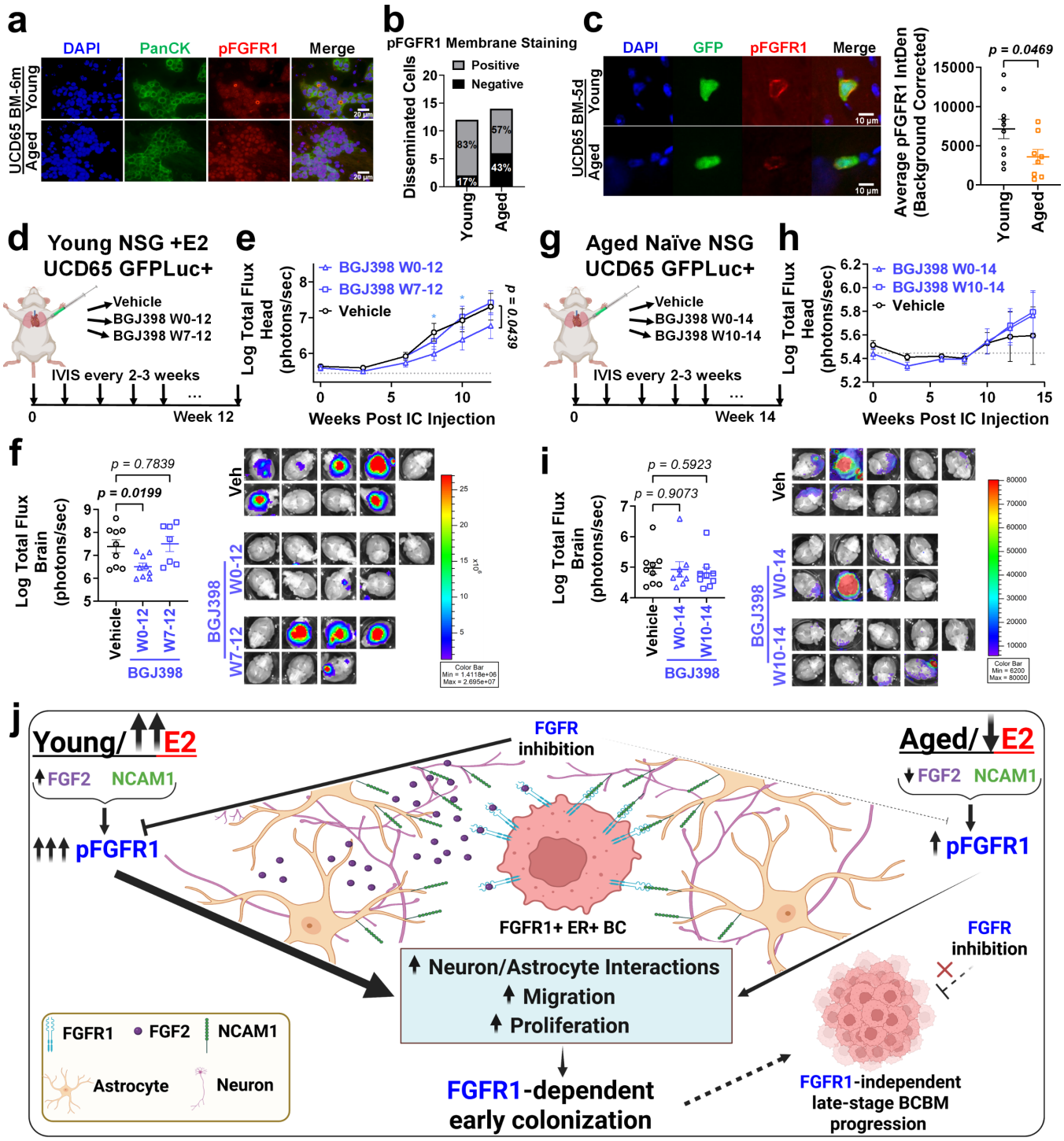

Fig. 8: FGFR1 kinase inhibition is only effective in early BCBM in young hosts

a, IF staining of PanCK and pFGFR1 in brain metastases from UCD65 cells in young (<15w) and aged (>60w) NSG mice, 6 months post-intracarotid injection. **b,** pFGFR1 quantification in brain disseminated UCD65 cells 5 days after intracardiac injection in young (<12w) and aged (>56w) NSG mice. Graph shows number and percentage of brain disseminated cells with positive membrane pFGFR1 staining. **c,** Average pFGFR1 intensity in GFP+ ROIs (n=8-10 images per group) corrected by background (GFP-). Data analyzed by Welch's t-test. **d,** UCD65 GFPLuc+ cells were injected intracardially into OVX young (<18w) NSG mice treated with E2 and randomized to receive vehicle (1% CMC, n=11) or BGJ398 (30mg/kg) 5x/week PO starting at the time of injection (W0-12, n=9) or 7 weeks post-ic (W7-12, n=11). **e,** Log-transformed head metastatic burden over time measured by IVIS. **f,** Log-transformed *ex vivo* brain metastatic burden at endpoint, measured by IVIS and images of all brains. **g,** UCD65 GFPLuc+ cells were injected intracardially into aged (>52w) NSG mice and mice randomized to receive vehicle (1% CMC, n=9) or BGJ398 (30mg/kg) 5x/week PO starting at the time of injection (W0-14, n=9) or 10 weeks post-injection (W10-14, n=9). **h,** Log-transformed head metastatic burden measured by IVIS. **i,** Log-tranformed *ex vivo* brain metastatic burden at endpoint, measured by IVIS and images of all brains. **j,** schematic of proposed pathway. For **e,h**, data were analyzed with 2-way ANOVA or mixed-effects analysis followed by Fisher's LSD test. Significant p-values shown for last time point only. Gray dotted line denotes baseline IVIS signal from a tumor-free mouse. For **f,i**, data were analyzed with 1-way ANOVA followed by Fisher's LSD test.

428 puncta and the migration of BC cells along neuronal tracks suggest that these cancer-neuron and
429 FGFR1/NCAM1 interactions are implicated in the progression of ER+ BCBMs. FGFR1 KD impairing
430 ER+ BC cell migration along neurites further supports the notion that NCAM1/FGFR1 interaction is
431 critical for the ability of ER+ BC cells to adhere to neurons and astrocytes, particularly during the early
432 stages of BM colonization. FGFR1 KD UCD65 and UCD12 cells showed decreased brain signal (but
433 not extracranial signal) immediately following intracardiac injection, suggesting that FGFR1 interactions
434 with the brain TME are essential for early colonization or survival of disseminated cells upon arrival to
435 the brain. Yet, FGFR1 kinase inhibition was only effective only when administered at early stages of
436 BCBM colonization in young hosts with high levels of FGF2, suggesting that FGF2 but not NCAM1-
437 driven FGFR1 activation is susceptible to this FGFR kinase inhibitor. Further studies are needed to
438 determine whether therapeutic blockage of NCAM1/FGFR1 can be achieved with other FGFR1
439 inhibitors or increased brain-penetrance of these drugs[53].

440 Our studies also show that late-stage FGFR1+ ER+ BMs are transcriptionally similar in young and aged
441 mice, and FGFR1 activation no longer drives growth at later stages of metastatic progression. These
442 results may explain why clinical trials have shown that not all patients with ER+ BC receiving FGFR
443 inhibitors respond to treatment, and why FGFR1 amplification does not predict response to this
444 therapy[54]. Collectively, our work demonstrates that changes in the brain TME mediate FGFR1-
445 amplified ER+ BCBM progression through interactions with astrocytes and neurons, which are critical
446 for early brain metastatic colonization but not late progression. Importantly, our studies caution that
447 current strategies to block FGFR1 function are ineffective to block non-canonical functions of FGFR1,
448 particularly in aged/E2-suppressed hosts, and suggest that accounting for host-specific FGFR1
449 activation may better predict response to FGFR inhibitors than amplification status alone.

450 **MATERIALS AND METHODS:**

451 **Ethics Statement:** All animal experiments and procedures were performed in an AAALAC-accredited
452 facility and approved by the University of Colorado Denver | Anschutz Medical Campus Institutional
453 Animal Care and Use Committee and by the DOD Animal Care and Use Review Office. Archival de-
454 identified brain metastasis human samples were obtained under approved IRB protocols at the
455 University of Colorado.

456 **Patient samples:** ER+ BCBM (n = 45), including $ER^+/HER2^-$ (n = 30), $ER^+/HER2^+$ (n = 14), and
457 $ER^+/PR^+/HER2^+$ (n = 1) from archival de-identified human brain metastases samples were obtained
458 under secondary use Colorado Multiple Institutional Review Board (COMIRB) protocol 23-1713 from
459 the University of Colorado tissue biorepository (waiver of consent COMIRB protocol 15-1461).

460 **Cell Lines and Culture:** ER+ cell lines UCD4, UCD12, and UCD65[38] were cultured in DMEM/F12 with
461 10% FBS, P/S, 100ng/mL cholera toxin, and 1nM insulin. MCF7 (FGFR1-OE and EV) were cultured in
462 MEM with EBSS, 10% FBS, P/S, 1x MEM amino acid solution, 1x MEM non-essential amino acids, and
463 1mM sodium pyruvate. SH-SY5Y cells were purchased from the Cell Technologies Shared Resource
464 (RRID: SCR_021982) and maintained in DMEM/F12 with 10% FBS and P/S. Human astrocytes (Cat.
465 #1800) were purchased from ScienceCell™ Research Laboratories and maintained in astrocyte
466 medium (AM, Cat. #1801) in flasks coated with Poly-L-Lysine (1ug/ml). Estrogen-free variations of all
467 medias were created using phenol red-free media base and 2-5% charcoal-stripped FBS. Starvation
468 media were created using phenol red-free media, no FBS, and 0.1% BSA.

469 ***In vivo* modeling of ER+ BC metastases:** Since circulating levels of E2 in gonadal intact young-female
470 mice (2.7± 1 pg/ml) are similar to those of post-menopausal women (1.3-4.9 pg/ml)[10], we mimicked post-
471 menopausal BC using naïve (non-operated) or sham-operated aged females[11]. To study brain metastatic
472 colonization, we use well recognized experimental models of metastasis, where cells are injected
473 intracardially or in the carotid artery to bypass the exit from primary tumor and allow studies of seeding
474 and metastatic colonization in the brain[32,55-57]. 500,000 cells were injected into the left ventricle of female
475 NSG mice. Intracarotid artery injections were performed as previously described[55]. Spontaneous
476 metastasis models were generated by injecting cells into the mammary fat pad of OVX NSG mice
477 supplemented with E2. Tumors were removed after reaching 1 cm^3, and mice were randomized into
478 indicated groups. Injection success and luciferase-transfected cell growth were tracked via live
479 bioluminescence imaging (BLI) using an IVIS® Spectrum optical scanner following subcutaneous
480 injection of luciferin substrate. For spontaneous models, the primary tumor site was covered during BLI
481 measurements. BLI measurements included tumor-free mice to establish background. For mice treated
482 with BGJ398 (Selleck Chemicals S2183), aliquots of drug were prepared daily and delivered via oral
483 gavage of 100µL in 1% CMC. Drug and vehicle were provided 5 times weekly.

484 **Magnetic Resonance Imaging (MRI) and Analysis:** To assess metastatic spread non-invasively, mice
485 underwent MRI XX weeks after tumor cell injection. Brain MRI was performed on anesthetized mice
486 (1.5% isoflurane) using a 9.4 Tesla BioSpec animal MRI scanner (Bruker Medical, Billerica, MA)
487 equipped with a 4-chanel phase-array mouse brain coil at the Colorado Animal Imaging Shared
488 Resource (AISR). Each MRI session consisted of a tri-pilot localizer, followed by a high resolution T2-
489 weighted fast spin echo (T2-turboRARE: field of view = 3 × 3 cm; repetition time = 4000ms; echo time =
490 80ms; slice thickness = 0.7 mm; 256 × 256 matrix size; 4 averages) with a 52-micron in-plane
491 resolution[58,59].

492 Total acquisition time for all sequences was 12 min 21 sec. The total metastatic gross volumes were
493 quantified by placing hand-driven region of interest (ROI) on sequential axial and/ or sagittal T2-
494 turboRARE images, summing total ROI areas and multiplying by 0.7 mm slice thickness (reported in
495 mm3). The largest diameters of larger metastatic lesions were also reported for axial MR images. All

496 MR image acquisition and analysis were performed using Bruker ParaVision 360neo v3.3 software. All
497 image analysis was performed by an MRI physicist with >15 years of experience (NJS).

498 **Immunoblots:** Membranes were blocked with 3% BSA in TBST and probed overnight with antibodies
499 against FGFR1 (Abcam ab76464), pFGFR1 (Y654, Abcam ab59194; Y653/Y654, Cell Signaling
500 52928S), Akt (Cell Signaling 9272S), pAkt (S473, Cell Signaling 4060S), ERK (Cell Signaling 9102S),
501 pERK (T202/T204, Cell Signaling 9101S), and NCAM1 (R&D AF2408), with GAPDH (Cell Signaling
502 97166S) or Tubulin (Sigma T5168) as loading controls. Membranes were washed with TBST and
503 probed with secondary antibodies (Invitrogen A11371, A21109, A21058, A21084, A11374) for 1-2hrs.
504 Blots were imaged on LiCor Odessey CLx and analyzed with ImageStudio Version 5.0 and 6.0. For
505 multiple stains, blots were stripped (Millipore 2504) and reprobed as above.

506 **qRT-PCR:** RNA was isolated with Trizol Reagent (Invitrogen 15596026) and reverse transcribed with
507 Verso cDNA Synthesis Kit (Thermo AB-1453). cDNA was used to perform qPCR with PowerUp SYBR
508 Green Master Mix (Applied Biosystems A25742) on Applied Biosystems QuantStudio 6 Flex. Gene
509 expression was calculated via ddCt. Primer Sequences:

510 *FGFR1* (F: AACCTGACCACAGAATTGGAGGCT, R: TGCTGCCGTACTCATTCTCCACA)

511 *NCAM1* (F: AATTTACCGCGGCAAGAACATC, R: CCTGGCTGGGAACAATATCCAC)

512 *RPLP0* (F: GTGATGTGCAGCTGATCAAGACT, R: GATGACCAGCCCAAAGGAGA)

513 **Primary Astrocyte Culture and Co-culture:** Brains from P0-P1 CD1 mouse pups were dissected, and
514 primary astrocytes were isolated and cultured as previously described[60]. For co-culture experiments,
515 50,000 or 10,000 cancer cells were seeded into 6-well or 24-well plates coated with laminin (1µg/ml),
516 respectively, onto astrocyte monolayers at 100% confluence in E2-free medium (DMEM/F12 phenol
517 red-free, supplemented with 5% charcoal-stripped FBS, 0.1% BSA, 1x penicillin/streptomycin, 1x non-
518 essential amino acids, 1x sodium pyruvate, and 1 nM insulin). Aged mouse astrocytes (aged-mAst)
519 were generated by maintaining cultures in growth medium (DMEM + 10% FBS, 1% P/S) for three
520 months prior to co-culture[61]. In contrast, mAst P0 refers to astrocytes maintained *in vitro* for only 8
521 days. For co-culture with human astrocytes, cells were seeded under the same conditions as murine
522 astrocytes. To generate 10x or 20x concentrated astrocyte-conditioned media (CM), confluent astrocyte
523 cultures were incubated for 72 hours in serum-free, phenol red-free DMEM/F12. Supernatants were
524 then collected and concentrated using 3,000Da molecular weight centrifugal filters.

525 **Isolation of Primary Cells from Adult Mouse Brain:** Whole brain tissue was dissected from young
526 (12 weeks) and aged (>56 weeks) female NSG mice following PBS cardiac perfusion. Cell suspensions
527 were obtained via enzymatic dissociation using the Papain Dissociation System (Worthington
528 Biochemical, LK003150), followed by magnetic-activated cell sorting (MACS; Miltenyi Biotec) according
529 to the manufacturer's instructions. Cell-type-specific isolation was performed using the following
530 reagents from Miltenyi Biotec: Myelin Removal Beads II (130-096-733) for oligodendrocytes, CD11b
531 MicroBeads (130-093-634) for microglia, Anti-ACSA-2 MicroBeads (130-097-678) for astrocytes, and
532 the Neuron Isolation Kit (130-115-389) for neurons.

533 **FGF2 ELISA:** Levels of FGF2 were quantified using the Mouse/Rat FGF basic/FGF2/bFGF Quantikine
534 ELISA Kit (R&D Systems, MFB00) according to the manufacturer's instructions.

535 **Lentivirus Production/Infection:** The following shRNA plasmids were purchased from the Functional
536 Genomics Shared Resources (RRID:SCR_021987): TRCN0000121186, TRCN0000000419, and
537 TRCN0000000418 targeting human FGFR1; TRCN0000373085 and TRCN0000373034 targeting
538 human NCAM1. MISSION® shRNA Plasmid DNA Control Vectors SHC216 and SCH002 were
539 purchased from Sigma. Lentiviral particles were produced in 293-T cells and concentrated via

ultracentrifugation. Viral particles were added to cells with 6μg/mL polybrene and selected with 2μg/mL puromycin.

Organotypic Co-culture: GFP+ cancer cells were cultured in ultra-low attachment plates to form spheroids. NSG mice were sacrificed and brains excised, sectioned into 250μm coronal slices, and collected in 1x HBSS with 2.5mM HEPES, 30mM D-Glucose, 1mM CaCl2, 1mM MgSO4, and 4mM NaHCO3 (Complete HBSS). Slices were plated in 12-well transwells. 1mL of media containing 25% complete HBSS, 25% donor equine serum, 50% MEM, 1x GlutaMAX (Gibco 35050061), and P/S was added to the well below the transwell. Spheroids of cancer cells were plated on top of the brain slices in <2μL media. Spheres were allowed to settle for 24 hours and images were acquired via stereo fluorescent microscopy every 48 hours. Growth was quantified via GFP intensity corrected for background autofluorescence of adjacent brain tissue (ImageJ).

Immunohistochemistry and Immunofluorescence: Formalin-fixed, paraffin-embedded sections of ER^+ BCBM from patient samples obtained at the University of Colorado were deparaffinized in xylene and rehydrated through a graded ethanol series to distilled water. Heat-induced antigen retrieval was performed in 10 mM citrate buffer (pH 6.0) or Tris-EDTA buffer (pH 9.0) at 125 °C and 25 psi for 10 minutes. Endogenous peroxidase activity was quenched with 3% hydrogen peroxide, and sections were blocked with 10% normal horse serum (ImmPRESS, Vector Laboratories). Slides were incubated overnight at RT with primary antibodies against FGFR1 (Invitrogen PA5-25979) or pFGFR1 (Y654, Abcam ab59194), followed by HRP-conjugated anti-rabbit IgG (ImmPRESS, Vector Laboratories). Signal was developed using 3,3′-diaminobenzidine (DAB; DAKO). Slides were scanned using an Aperio ScanScope T3 (Leica Biosystems), and membrane expression of FGFR1 and pFGFR1 in tumor cells was quantified using the Aperio Image Analysis software.

For immunofluorescence, cells grown on coverslips and free-floating brain slices were fixed with 4% paraformaldehyde (PFA) and heat-induced antigen retrieval was performed in boiling 10 mM citrate buffer (pH 6.0). Coverslips, slices, or deparaffinized formalin-fixed, paraffin-embedded sections (as described above), were blocked with 10% normal donkey serum (NDS) in TBST for 1 hour at RT. Primary antibodies against GFAP (Invitrogen 12-0300), FGF2 (Novusbio NBP3-15367), pFGFR1 (Y654, Abcam ab59194), NCAM1 (R&D AF2408), PanCK (DAKO M0821), Synapsin1/2 (Synaptic Systems 106004), and PSD95 (Invitrogen MA1-045) were incubated for 2 hours or overnight at RT. For double staining, primary antibodies were applied either sequentially in separate incubations or pooled. After washing with PBS containing 0.01% Triton X-100, coverslips, slices, or slides were incubated with secondary antibodies (Jackson ImmunoResearch 712-545-153, 712-585-153, 706-165-148, 715-545-150, 715-585-150, 715-605-150, 705-585-147, 711-545-152, 711-585-152, 711-605-152) diluted in TBST for 2 hours at RT in the dark. Nuclei were stained with DAPI (1 μg/mL in methanol or PBS) for 10 minutes at RT and samples were mounted with FluoroMount-G (Southern Biotech).

Growth Assays: Cells were maintained in E2-free media for 48 hours before being trypsinized with phenol red-free trypsin and plated at densities of 2,000 MCF7, 10,000 UCD12, and 20,000 UCD65 cells per well of duplicate 96-well plates in 100μL of media. Following 24 hours, 100μL of media containing each treatment (2x) was added to the wells of one plate. The duplicate plate was fixed with 10% TCA. Growth was tracked via Incucyte S3 system where 10x phase contrast and GFP images were obtained every 12 hours. Treatments were maintained by regularly changing 50% of media. At the conclusion of the Incucyte tracking, plates were fixed with 10% TCA. Fixed plates were stained with 0.04% SRB (Sigma) and total protein was quantified via plate reader measurements at 565, 525, and 490nm subtracting 690nm background. Proliferation was additionally measured by quantifying fold change of SRB signal between the two plates.

585 **Digital Spatial Transcriptomics:** Female NSG mice were ovariectomized or sham operated and 15
586 days later injected via intracarotid artery with 250,000 UCD65 GFPLuc+ cells. Mice were classified
587 according to their age as young (between 7 and 15 weeks) or aged (>60 weeks). Development of brain
588 metastasis was monitored during 15 weeks via IVIS. Six months after injection, animals were
589 euthanized by ketamine/xylazine overdose and perfused with PBS/4%PFA. Brains were cryopreserved
590 in 20% sucrose and stored at 4°C. Paraffin embedded fixed coronal sections were stained with
591 antibodies targeting PanCK (DAKO M0821), Iba1 (WAKO PTG5394), GFAP (Invitrogen 13-0300) and
592 DAPI. One set of brain sections from young-sham, aged-sham, young-OVX and aged-OVX mice were
593 probed by in situ hybridization with the GeoMx® Mouse Whole Transcriptome Atlas (WTA) library. Then,
594 using the GeoMX Digital Spatial Profiler (DSP), barcoded RNA-probes in the Iba+/GFAP+ regions of
595 interest (ROI) surrounding PanCK+ brain metastases were UV-cleaved and processed by Illumina
596 sequencing. Similarly, another set of brain sections from young-sham and aged-sham mice were
597 probed by in situ hybridization with the GeoMx® Human WTA library. Then, with the GeoMX DSP, RNA-
598 probes in the PanCK+ ROIs (human breast cancer cells) were UV-cleaved and processed by Illumina
599 sequencing. A total of 48 Iba+/GFAP+ ROIs (young-sham = 18, aged-sham = 16, young-OVX = 9, and
600 aged-OVX = 5) and 59 PanCK+ ROIs (aged-sham = 16 and young-sham = 43) were retrieved and
601 sequenced using an Illumina NovaSeq X plus sequencer in one lane on a 10B flow cell at 2x150bp
602 configuration. Sequencing was performed by the Genomics Shared Resource (RRID: SCR_021984).

603 Using the GeoMx® NGS Pipeline (Nanostring) and the Probe Kit Configuration (PKC) files for Human
604 or Mouse RNA WTA, the FASTQ libraries were processed to obtain the Digital Count Conversion (DCC)
605 files. DCC files were analyzed in R (4.4.2) with NanoStringNCTools[62], GeomxTools[63] and
606 GeoMxWorkflows[64] packages. All ROIs with gene detection rate (defined as the number of genes in the
607 sample divided by the number of genes in the WTA) above 1%, more than 100 nuclei, and all probes in
608 the highest quartile above the background reading were retained for further analysis (**Supplementary**
609 **Fig. 3**). Raw counts were normalized using the Q3 method in NanoStringNCTools. Normalized counts
610 were used to UMAP analysis with the umap package in R. Differential expression analyses were
611 performed with limma-voom in standR[65,66] using the GeoMXAnalysisWorkflow package in R[67].
612 Differentially expressed genes were visualized as MA plots with ggplot2.

613 Log-CPM (counts per million) values were transformed with “voom” to get the appropriate observation-
614 level weights and fitted to a linear model with “fit”. Then using “contrasts.fit”, the array was used to get
615 estimated coefficients and standard errors for each pairwise comparison. Finally, the differential
616 expression statistics were computed using empirical Bayes moderation with “ebayes”. Differentially
617 expressed genes lists were used to perform a gene sets enrichment analysis (GSEA) following the
618 GeoMXAnalysisWorkflow method[67]. Briefly, MSigDB Hallmarks, MSigDB C2, Gene Ontology and
619 KEGG databases were downloaded in R using the msigdb and GSEABase libraries[68,69]. Enrichment
620 analyses were performed using fry from the limma package[66]. Finally, using vissE package[70] we
621 clustered significant (FDR <0.05) enriched gene sets based on the genes overlap with a threshold of
622 35%. Clusters were further analyzed by text mining to identify common biological patterns using the
623 gene set names. Additionally, frequency of each gene in each cluster was plotted vs their respective
624 $\log_2$FC. Clusters were ranked by size and FDR and top 9 clusters were plotted using igraph[71].

625 **Mammosphere formation assay:** A total of 750 UCD65 cells were suspended in 50 µL of phenol red-
626 free DMEM/F12 with heparin (4µg/ml), hydrocortisone (1µg/ml), cholera toxin (100ng/ml), and 1%
627 methylcellulose and plated in ultra-low attachment 96-well plates. An additional 50 µL of treatments
628 (starvation media, 20X astrocyte-conditioned media, or 20X aged astrocyte-conditioned media) were
629 added. Mammosphere media without CM treatments were additionally supplemented with bFGF
630 (20ng/mL), EGF (20ng/mL), and 1x B-27 (Gibco 17504044). Whole-well images were captured every
631 12 hours for 20 days using the Incucyte S3 system. Mammospheres (green mask) were analyzed using

632 the "analyze particles" command in ImageJ, with the parameters set to an area ≥ 200 μm² and
633 circularity between 0.5 and 1.

634 **Recombinant protein treatment for downstream signaling**: 1 million UCD65, UCD12, or MCF7 cells
635 were plated in 60cm plates. 12 hours after plating, cells were washed three times with PBS and media
636 was replaced with starvation media. Following 48-72 hours in starvation media, media was replaced
637 with starvation media containing the indicated concentrations of FGF2 (PeproTech AF-100-18B) or
638 NCAM1 (Acro Biosystems NC1-H5223). Pretreatments with BGJ398 (Selleck Chemicals S2183) or
639 Ponatinib (Selleck Chemicals S1490) were completed 1 hour prior to treatments. Following treatment,
640 protein was collected in RIPA buffer.

641 **RNA Sequencing**: UCD65 and UCD12 cells were serum-starved and then treated with vehicle,
642 10ng/mL FGF2, or 20ug/mL for 24hr. RNA was isolated with Trizol Reagent (Invitrogen 15596026)
643 followed by RNeasy Cleanup Kit (Qiagen 74204). mRNA libraries were created using poly-A enrichment
644 and sequenced at 40M PE150 reads by NovaSeq X Plus Series (Illumina). Reads were filtered by
645 quality (removal of reads containing adaptors, >10% undetermined bases, and QScore <5 for 50% of
646 bases) and aligned with HiSAT2 (2.2.1) to Homo Sapiens Reference Genome (GRCh38/hg38). Raw
647 counts were obtained with featureCounts (2.0.6), and analyzed in R 4.5.0. Normalized counts and
648 differential expression were obtained with deseq2[72] and used to perform gene sets enrichment analysis
649 (GSEA) as described above for digital spatial transcriptomics, clustered based on 25% gene overlap.

650 **Primary Neuron Culture and Co-Culture:** Hippocampi were dissected from P0-1 CD1 pups and
651 neurons were isolated as previously described[73]. Primary neurons were cultured on poly-l-lysine coated
652 coverslips in 24-well plates and maintained in phenol red-free neurobasal media supplemented with
653 GlutaMAX, 1x B27, and P/S, with 50% media replaced twice weekly. Five days after isolation, 1.5μM
654 cytosine arabinoside was added to each well. After 48 hours, 50% media was replaced. For co-cultures,
655 5,000-10,000 cancer cells were added to each well 24 hours after cytosine arabinoside removal. Co-
656 cultures grew for 5-10 additional days before coverslips were fixed.

657 **Synapse Detection and Quantification:** Synapsin1/2 and PSD95 were costained via
658 immunofluorescence and samples were imaged via confocal microscopy (3I MARIANAS Inverted
659 Spinning Disk) at 40x magnification. SynQuant ImageJ plugin[74] was used to quantify synapses as
660 punctate co-localization of the two markers, and synapse number was controlled for analysis area
661 differences between images.

662 **Neural Migration Analysis:** Phase and GFP images were collected every 12 hours. GFP+ ROIs were
663 defined to indicate cells in each image. Using ImageJ, phase images were used to stabilize motion
664 across time points[75], and these corrections were applied to the GFP+ ROIs. Movement was tracked
665 using TrackMate[76,77].

666 **Statistical Analysis and Reproducibility:** Statistical analyses are specified in figure legends and were
667 performed with GraphPad Prism 10.4.2 for predetermined comparisons only. All tests were 2-tailed.
668 Statistical analysis of sequencing data was performed in R 4.4.2 and 4.5.0. For animal experiments
669 involving injections of different cells, groups were littermate-matched and injections were blinded. For
670 treatment of established tumors, groups were randomized. In studies involving aged mice, there was
671 expected age-related, non-tumor related mortality. These animals were excluded from final analysis
672 and initial group sizes were 20% larger to account for this loss. Where possible, analyses were blinded
673 to experimental conditions or performed using automated functions to reduce bias.

674 **Data Availability:** Digital Spatial Profiling and RNA-sequencing data will be uploaded to NCBI's Gene
675 Expression Omnibus prior to publication.

676 **Code Availability:** All information is provided in the Methods, including packages, software, and
677 pipelines. No custom code was generated during these studies.

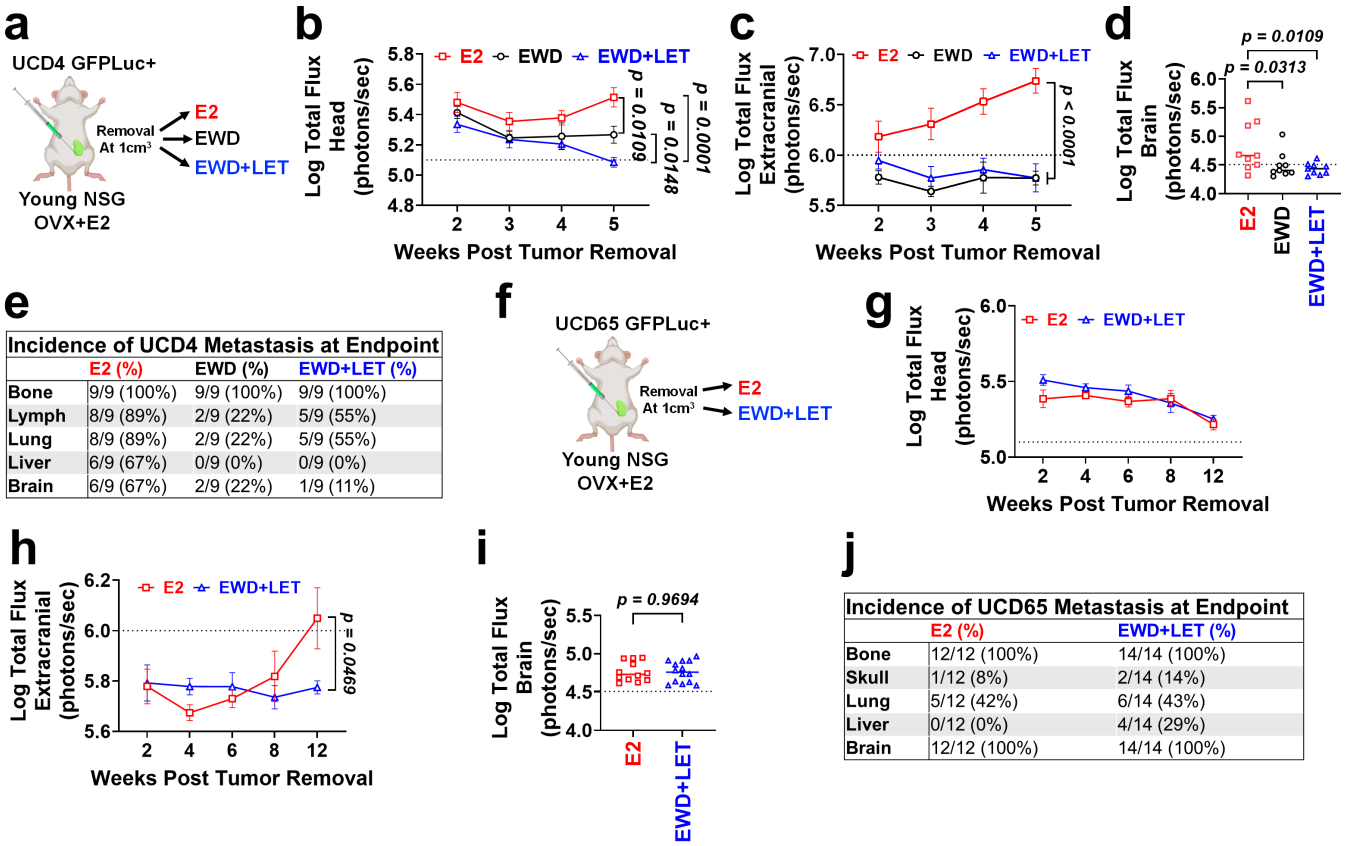

Incidence of UCD4 Metastasis at Endpoint			
	E2 (%)	EWD (%)	EWD+LET (%)
Bone	9/9 (100%)	9/9 (100%)	9/9 (100%)
Lymph	8/9 (89%)	2/9 (22%)	5/9 (55%)
Lung	8/9 (89%)	2/9 (22%)	5/9 (55%)
Liver	6/9 (67%)	0/9 (0%)	0/9 (0%)
Brain	6/9 (67%)	2/9 (22%)	1/9 (11%)

Incidence of UCD65 Metastasis at Endpoint		
	E2 (%)	EWD+LET (%)
Bone	12/12 (100%)	14/14 (100%)
Skull	1/12 (8%)	2/14 (14%)
Lung	5/12 (42%)	6/14 (43%)
Liver	0/12 (0%)	4/14 (29%)
Brain	12/12 (100%)	14/14 (100%)

Extended Data Fig. 1: Spontaneous metastases models of ER+ breast cancer result in E2-dependent dissemination and outgrowth of metastases, as well as E2-independent metastatic progression in a subset of mice.
a, UCD4 GFPLuc+ cells were injected into the mammary fat pad (MFP) of young NSG mice supplemented with pre-menopausal levels of E2. Tumors were removed at 1cm^3 and mice were randomized to keep receiving E2 (n=9), undergo E2-withdrawl (EWD, n=9), or EWD+ letrozole (LET, n=9). **b,** Log-transformed head metastatic burden over time, measured by IVIS. **c,** Log-transformed overall metastatic dissemination over time, measured by IVIS. **d,** *Ex vivo* IVIS signal in the brain at endpoint. **e,** Quantification of metastasis incidence at multiple distant sites at endpoint. **f,** UCD65 GFPLuc+ cells were injected into the MFP of young NSG mice supplemented with E2. Tumors were removed at 1cm^3 and mice were randomized to keep receiving E2 (n=12), or to undergo E2-withdrawl (EWD)+ letrozole (LET, n=14). **g,** Log-transformed head metastatic burden over time, measured by IVIS. **h,** Log-transformed extracranial metastatic dissemination over time, measured by IVIS. **i,** *Ex vivo* IVIS signal in the brain at endpoint. **j,** Quantification of metastasis frequency at multiple sites at endpoint. For **b,c,g,h** , lines denote mean ± SEM. Data were analyzed with 2-way ANOVA or mixed-effects analysis followed by Fisher's LSD test. P-value shown for last time point for all values <0.05. **d** was analyzed with one-way ANOVA followed by Fisher's LSD test. **i** was analyzed with an unpaired student's t-test. Gray dotted line denotes baseline IVIS signal from a tumor-free mouse.

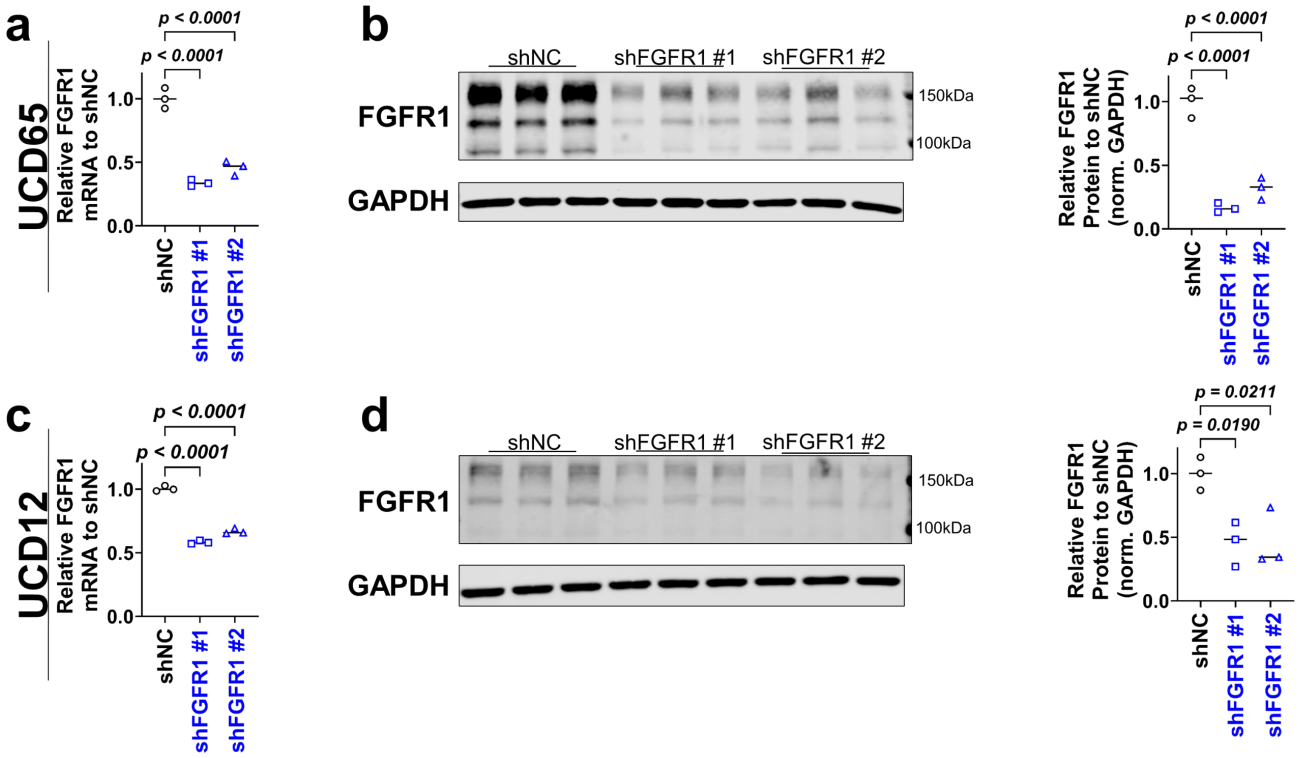

692 **Extended Data Fig. 2. FGFR1 is successfully downregulated in UCD65 and UCD12 cells.**
693 **a,** RT-qPCR of FGFR1 mRNA in shNC and shFGFR1 UCD65 cells (n=3 replicates). **b,** Immunoblot of FGFR1 and
694 quantification of FGFR1 normalized to GAPDH relative to shNC from 3 biological replicates of shNC and shFGFR1 UCD65
695 cells. **c,** RT-qPCR of FGFR1 mRNA in shNC and shFGFR1 UCD12 cells (n=3 replicates). **d,** Immunoblot of FGFR1 and
696 quantification of FGFR1 normalized to GAPDH relative to shNC from 3 biological replicates of shNC and shFGFR1 UCD12
697 cells. All data analyzed by 1-way ANOVA followed by Fisher's LSD test.

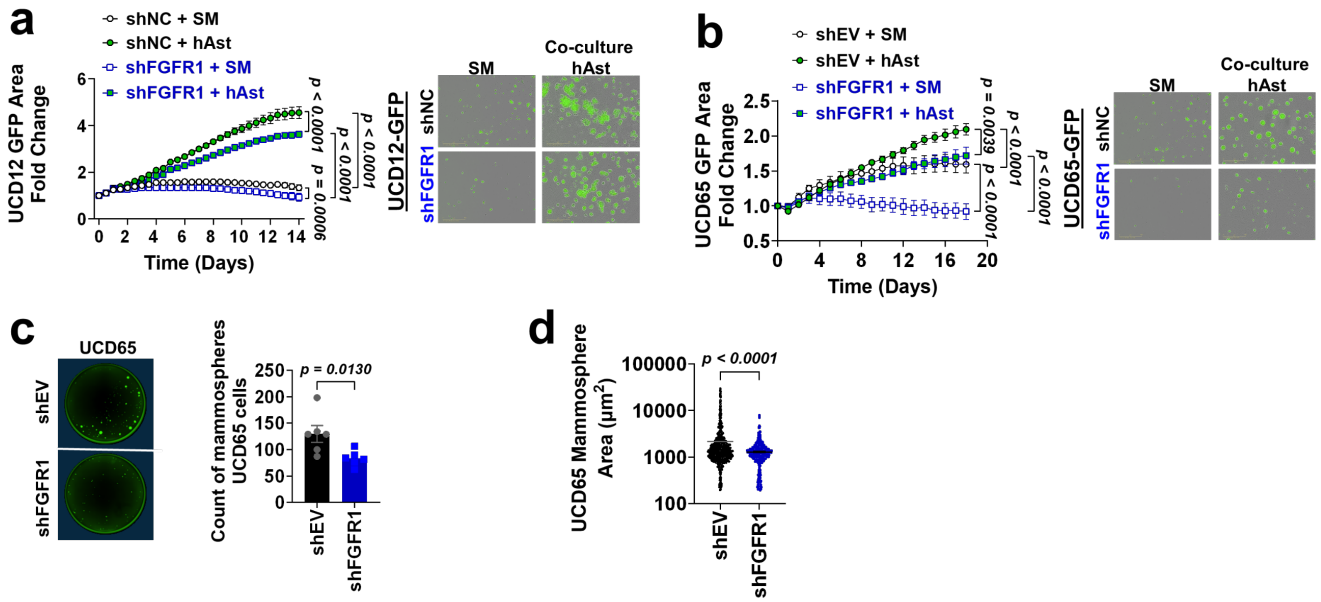

Extended Data Fig. 3: Contribution of FGFR1 and human astrocyte co-culture to ER⁺ cancer cell proliferation and tumor-initiating capability.

shNC or shFGFR1 UCD12-GFP+ (**a**, n=3 replicates per condition) and shEV or shFGFR1 UCD65-GFP+ (**b**, n=5-6 replicates per condition) cells were treated with starvation medium (SM) alone or co-cultured with human astrocytes (hAst, ScienceCell #1800-10). Graphs show fold change in total green area relative to time 0, measured by Incucyte. Right: Representative images of UCD12 cells at 14 days and UCD65 cells at 18 days for each condition. **c,** Representative image of UCD65-GFP+ cells 26 days after seeding 750 cells in a low-attachment 96-well plate with mammosphere culture media. Right: Total number of mammospheres (>200μm^2) of UCD65-GFP+ shEV and shFGFR1 cells at day 20 (n=6 plates). **d,** Number and area of mammospheres quantified across six separate 96-well plates for each cell line (n=498-774 mammospheres). Plot shows mammosphere area for UCD65 shEV and shFGFR1 cells. Data in **a,b** were analyzed with 2-way ANOVA followed by Fisher's LSD test. Data in **c,d** were analyzed by Mann-Whitney test.

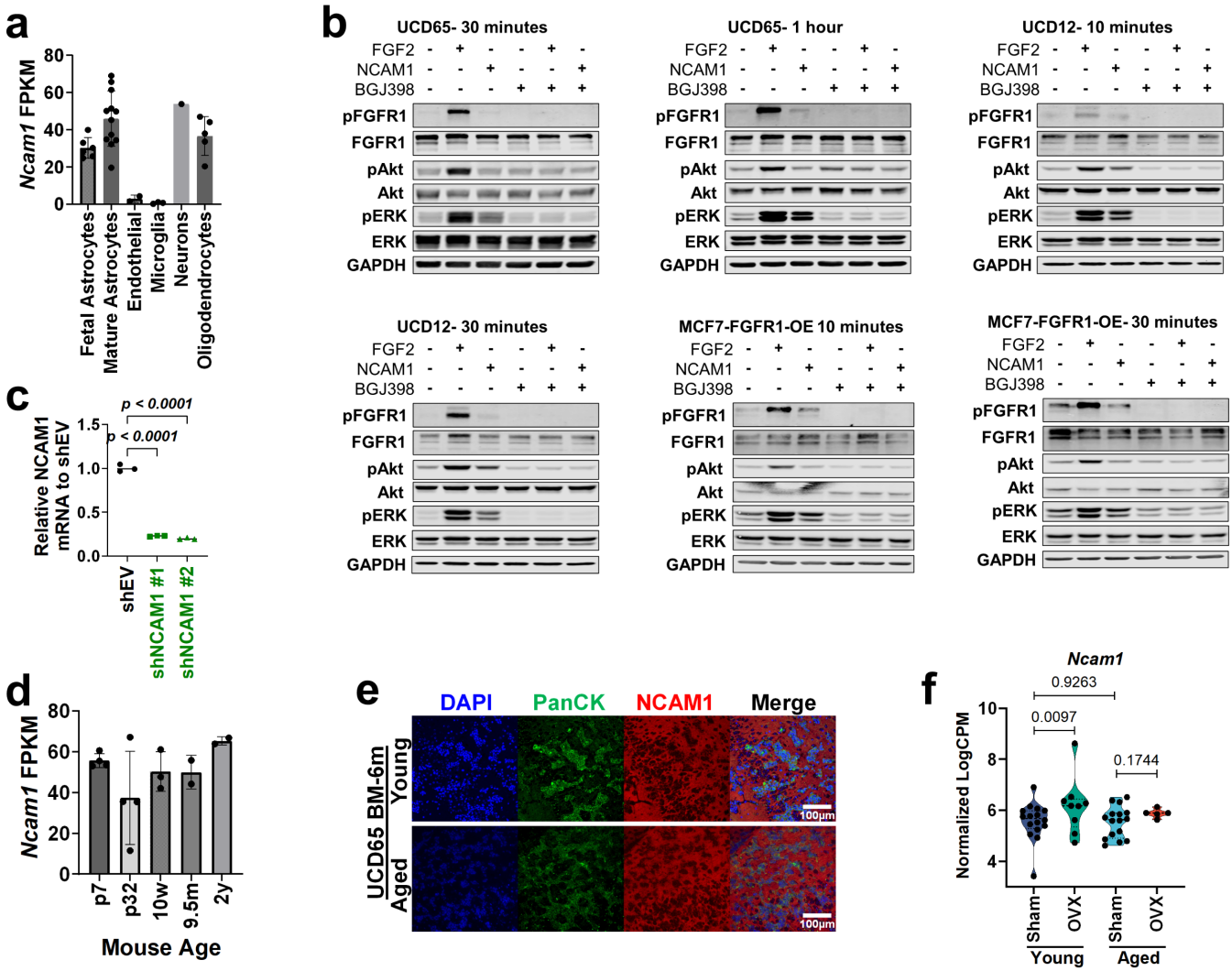

Extended Data Fig. 4: NCAM1 signaling activation and expression

a, Expression of NCAM1 mRNA in human brain cells as reported from brainrnaseq.org[78]. **b,** UCD65, UCD12, and MCF7 FGFR1-OE cells were pretreated with 10µM BGJ398 or vehicle for 1 hour, then treated with 10ng/mL FGF2, 250nM NCAM1, or vehicle for the indicated times. WBs of pFGFR1, FGFR1, pAkt, Akt, pERK, ERK, and GAPDH. **c,** qPCR of NCAM1 in SY5Y shNCAM1 and shEV (n=3 replicates). 1-way ANOVA with Fisher's LSD test. **d,** NCAM1 mRNA expression in mouse astrocytes of different ages as reported at brainrnaseq.org[79]. **e,** IF staining of PanCK and NCAM1 in brain metastases from UCD65 cells injected via intracarotid artery in young (<15w) and aged (>60w) NSG mice, 6 months post-injection. **f,** Normalized Log2 counts per million (CPM) for NCAM1 in non-glial ROIs from NanoString dataset (**Fig. 4e**), analyzed with empirical bayes.

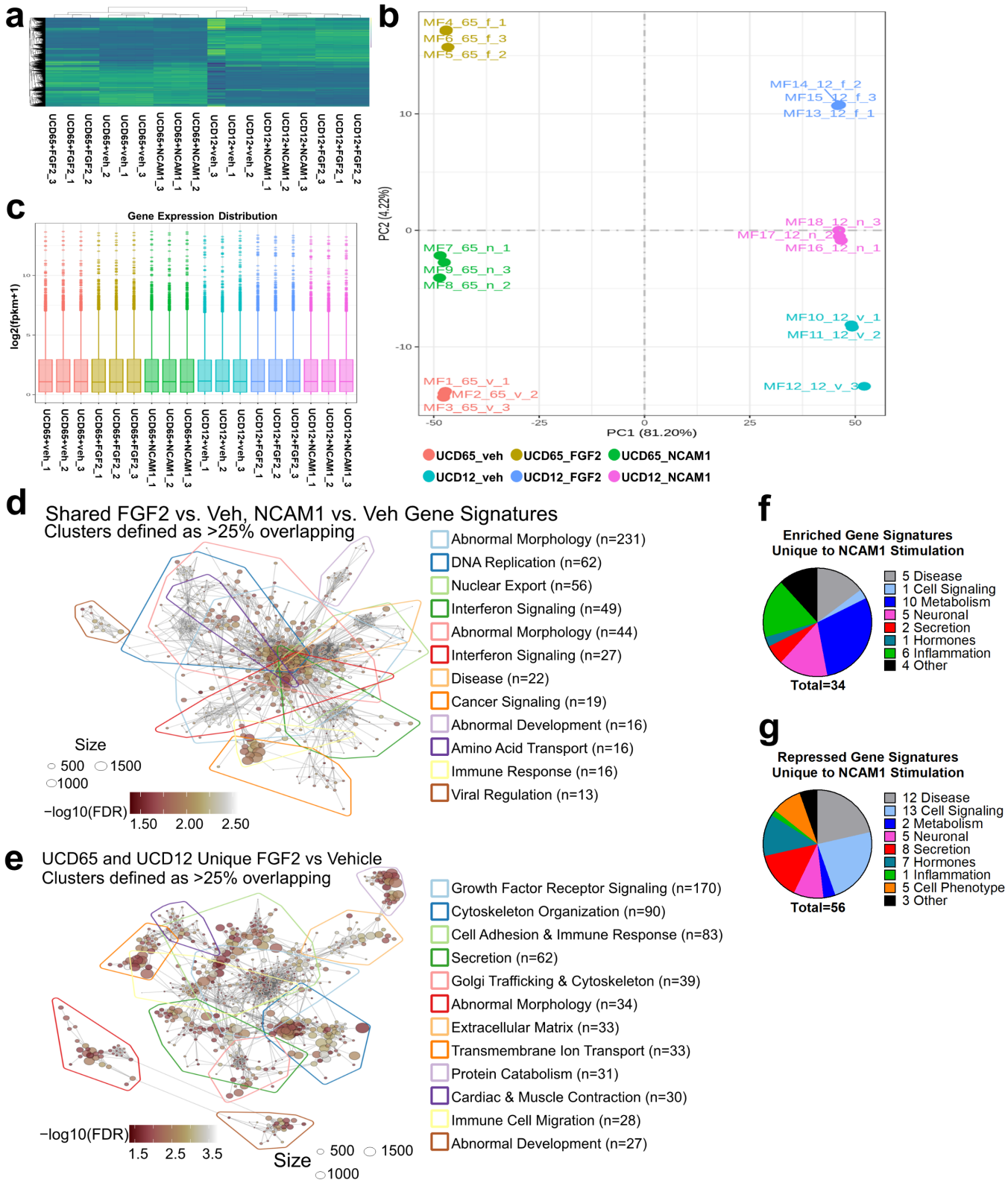

Extended Data Fig. 5: RNA sequencing and analysis of NCAM1 and FGF2 treatments in UCD12 and UCD65 cells. **a,** Clustering of samples by normalized expression (z-score of normalized counts) demonstrates grouping by cell line and treatment. **b,** Principal component analysis (PCA) of gene expression values (FPKM) for each sample. **c,** Distribution of gene expression levels for each sample. **d,** Top 12 significant differentially expressed clusters of pathways (defined as signatures sharing >25% overlapping genes) for gene sets shared between FGF2_vs_veh and NCAM1_vs_veh. **e,** Top 12 significant differentially expressed clusters of pathways (defined as signatures sharing >25% overlapping genes) for gene sets unique to FGF2_vs_veh. **f,** Categorized gene signatures enriched following NCAM1 treatment. **g,** Categorized gene signatures repressed following NCAM1 treatment.

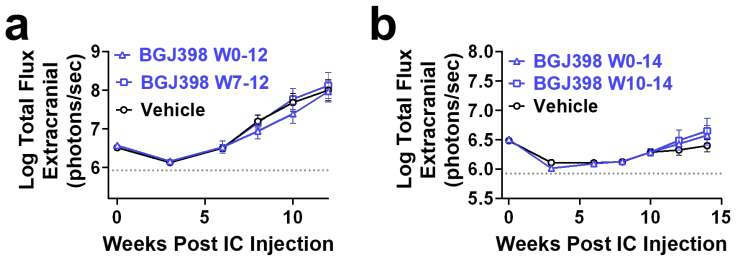

Extended Data Fig. 6: Extracranial growth of UCD65 cells following FGFR inhibition.
a, Log-transformed head metastatic burden over time in young mice supplemented with E2, measured by IVIS. **b,** Log-transformed head metastatic burden over time in aged naïve mice, measured by IVIS. Lines denote mean ± SEM. Data were analyzed with 2-way ANOVA followed by Fisher's LSD test.

730 **REFERENCES**

731 1 Kaal, E. C. A., Niël, C. G. J. H. & Vecht, C. J. Therapeutic management of brain metastasis. *The Lancet*
732 *Neurology* **4**, 289-298 (2005). https://doi.org/10.1016/S1474-4422(05)70072-7
733 2 Palmieri, D. *et al.* Brain metastases of breast cancer. *Breast disease* **26**, 139-147 (2006).
734 3 Morris, P. G. *et al.* Limited Overall Survival in Patients with Brain Metastases from Triple Negative Breast
735 Cancer. *The Breast Journal* **18**, 345-350 (2012). https://doi.org/10.1111/j.1524-4741.2012.01246.x
736 4 Press, D. J., Miller, M. E., Liederbach, E., Yao, K. & Huo, D. De novo metastasis in breast cancer:
737 occurrence and overall survival stratified by molecular subtype. *Clin Exp Metastasis* **34**, 457-465 (2017).
738 https://doi.org/10.1007/s10585-017-9871-9
739 5 Kennecke, H. *et al.* Metastatic behavior of breast cancer subtypes. *J Clin Oncol* **28**, 3271-3277 (2010).
740 https://doi.org/10.1200/JCO.2009.25.9820
741 6 Heitz, F. *et al.* Triple-negative and HER2-overexpressing breast cancers exhibit an elevated risk and an
742 earlier occurrence of cerebral metastases. *Eur J Cancer* **45**, 2792-2798 (2009).
743 https://doi.org/10.1016/j.ejca.2009.06.027
744 7 Chatzistamou, I. & Kiaris, H. Modeling estrogen receptor-positive breast cancers in mice: is it the best we
745 can do? *Endocr Relat Cancer* **23**, C9-C12 (2016). https://doi.org/10.1530/ERC-16-0397
746 8 Sledge, G. W. *et al.* Past, present, and future challenges in breast cancer treatment. *J Clin Oncol* **32**, 1979-
747 1986 (2014). https://doi.org/10.1200/JCO.2014.55.4139
748 9 Turrell, F. K. *et al.* Age-associated microenvironmental changes highlight the role of PDGF-C in ER(+)
749 breast cancer metastatic relapse. *Nat Cancer* **4**, 468-484 (2023). https://doi.org/10.1038/s43018-023-
750 00525-y
751 10 Rothman, M. S. *et al.* Reexamination of testosterone, dihydrotestosterone, estradiol and estrone levels
752 across the menstrual cycle and in postmenopausal women measured by liquid chromatography-tandem
753 mass spectrometry. *Steroids* **76**, 177-182 (2011). https://doi.org/10.1016/j.steroids.2010.10.010
754 11 Osborne, C. K., Hobbs, K. & Clark, G. M. Effect of estrogens and antiestrogens on growth of human breast
755 cancer cells in athymic nude mice. *Cancer Res* **45**, 584-590 (1985).
756 12 Offner, H. & Polanczyk, M. A potential role for estrogen in experimental autoimmune encephalomyelitis
757 and multiple sclerosis. *Ann N Y Acad Sci* **1089**, 343-372 (2006). https://doi.org/10.1196/annals.1386.021
758 13 Guerini-Rocco, E. *et al.* Genomic Aberrations and Late Recurrence in Postmenopausal Women with
759 Hormone Receptor-positive Early Breast Cancer: Results from the SOLE Trial. *Clin Cancer Res* (2021).
760 https://doi.org/10.1158/1078-0432.CCR-20-0126
761 14 DiGiacomo, J. W., Godet, I., Trautmann-Rodriguez, M. & Gilkes, D. M. Extracellular Matrix-Bound FGF2
762 Mediates Estrogen Receptor Signaling and Therapeutic Response in Breast Cancer. *Mol Cancer Res* **19**,
763 136-149 (2021). https://doi.org/10.1158/1541-7786.MCR-20-0554
764 15 Garcia-Recio, S. *et al.* FGFR4 regulates tumor subtype differentiation in luminal breast cancer and
765 metastatic disease. *J Clin Invest* **130**, 4871-4887 (2020). https://doi.org/10.1172/JCI130323
766 16 Formisano, L. *et al.* Aberrant FGFR signaling mediates resistance to CDK4/6 inhibitors in ER+ breast
767 cancer. *Nat Commun* **10**, 1373 (2019). https://doi.org/10.1038/s41467-019-09068-2
768 17 Drago, J. Z. *et al.* FGFR1 Amplification Mediates Endocrine Resistance but Retains TORC Sensitivity in
769 Metastatic Hormone Receptor-Positive (HR(+)) Breast Cancer. *Clin Cancer Res* **25**, 6443-6451 (2019).
770 https://doi.org/10.1158/1078-0432.CCR-19-0138
771 18 Ding, K. *et al.* FGFR4 in endocrine resistance: overexpression and estrogen regulation without direct
772 causative role. *Breast Cancer Res Treat* **211**, 501-515 (2025). https://doi.org/10.1007/s10549-025-07666-
773 x
774 19 Xie, N. *et al.* FGFR aberrations increase the risk of brain metastases and predict poor prognosis in
775 metastatic breast cancer patients. *Ther Adv Med Oncol* **12**, 1758835920915305 (2020).
776 https://doi.org/10.1177/1758835920915305
777 20 Wellberg, E. A. *et al.* FGFR1 underlies obesity-associated progression of estrogen receptor-positive breast
778 cancer after estrogen deprivation. *JCI Insight* **3** (2018). https://doi.org/10.1172/jci.insight.120594
779 21 Sytnyk, V., Leshchyns'ka, I. & Schachner, M. Neural Cell Adhesion Molecules of the Immunoglobulin
780 Superfamily Regulate Synapse Formation, Maintenance, and Function. *Trends Neurosci* **40**, 295-308
781 (2017). https://doi.org/10.1016/j.tins.2017.03.003

22 Dabrowski, A., Terauchi, A., Strong, C. & Umemori, H. Distinct sets of FGF receptors sculpt excitatory and inhibitory synaptogenesis. *Development* **142**, 1818-1830 (2015). https://doi.org/10.1242/dev.115568

23 Terauchi, A. *et al.* Distinct FGFs promote differentiation of excitatory and inhibitory synapses. *Nature* **465**, 783-787 (2010). https://doi.org/10.1038/nature09041

24 Umemori, H., Linhoff, M. W., Ornitz, D. M. & Sanes, J. R. FGF22 and its close relatives are presynaptic organizing molecules in the mammalian brain. *Cell* **118**, 257-270 (2004). https://doi.org/10.1016/j.cell.2004.06.025

25 Klimaschewski, L. & Claus, P. Fibroblast Growth Factor Signalling in the Diseased Nervous System. *Mol Neurobiol* **58**, 3884-3902 (2021). https://doi.org/10.1007/s12035-021-02367-0

26 Ohkubo, Y., Uchida, A. O., Shin, D., Partanen, J. & Vaccarino, F. M. Fibroblast growth factor receptor 1 is required for the proliferation of hippocampal progenitor cells and for hippocampal growth in mouse. *J Neurosci* **24**, 6057-6069 (2004). https://doi.org/10.1523/JNEUROSCI.1140-04.2004

27 Gonzalez, A. M., Berry, M., Maher, P. A., Logan, A. & Baird, A. A comprehensive analysis of the distribution of FGF-2 and FGFR1 in the rat brain. *Brain Res* **701**, 201-226 (1995). https://doi.org/10.1016/0006-8993(95)01002-x

28 Ma, D. K., Ponnusamy, K., Song, M. R., Ming, G. L. & Song, H. Molecular genetic analysis of FGFR1 signalling reveals distinct roles of MAPK and PLCgamma1 activation for self-renewal of adult neural stem cells. *Mol Brain* **2**, 16 (2009). https://doi.org/10.1186/1756-6606-2-16

29 Cambon, K. *et al.* A synthetic neural cell adhesion molecule mimetic peptide promotes synaptogenesis, enhances presynaptic function, and facilitates memory consolidation. *J Neurosci* **24**, 4197-4204 (2004). https://doi.org/10.1523/JNEUROSCI.0436-04.2004

30 Christensen, C., Berezin, V. & Bock, E. Neural cell adhesion molecule differentially interacts with isoforms of the fibroblast growth factor receptor. *Neuroreport* **22**, 727-732 (2011). https://doi.org/10.1097/WNR.0b013e3283491682

31 Kiselyov, V. V., Soroka, V., Berezin, V. & Bock, E. Structural biology of NCAM homophilic binding and activation of FGFR. *J Neurochem* **94**, 1169-1179 (2005). https://doi.org/10.1111/j.1471-4159.2005.03284.x

32 Kiselyov, V. V. *et al.* Structural basis for a direct interaction between FGFR1 and NCAM and evidence for a regulatory role of ATP. *Structure* **11**, 691-701 (2003). https://doi.org/10.1016/s0969-2126(03)00096-0

33 Krushel, L. A., Tai, M. H., Cunningham, B. A., Edelman, G. M. & Crossin, K. L. Neural cell adhesion molecule (N-CAM) domains and intracellular signaling pathways involved in the inhibition of astrocyte proliferation. *Proc Natl Acad Sci U S A* **95**, 2592-2596 (1998). https://doi.org/10.1073/pnas.95.5.2592

34 Kobayashi, S., Vidal, I., Pena, J. D. & Hernandez, M. R. Expression of neural cell adhesion molecule (NCAM) characterizes a subpopulation of type 1 astrocytes in human optic nerve head. *Glia* **20**, 262-273 (1997). https://doi.org/10.1002/(sici)1098-1136(199707)20:3<262::aid-glia10>3.0.co;2-s

35 Weledji, E. P. & Assob, J. C. The ubiquitous neural cell adhesion molecule (N-CAM). *Ann Med Surg (Lond)* **3**, 77-81 (2014). https://doi.org/10.1016/j.amsu.2014.06.014

36 Knafo, S. *et al.* Facilitation of AMPA receptor synaptic delivery as a molecular mechanism for cognitive enhancement. *PLoS Biol* **10**, e1001262 (2012). https://doi.org/10.1371/journal.pbio.1001262

37 Leshchyns'ka, I., Sytnyk, V., Morrow, J. S. & Schachner, M. Neural cell adhesion molecule (NCAM) association with PKCbeta2 via betaI spectrin is implicated in NCAM-mediated neurite outgrowth. *J Cell Biol* **161**, 625-639 (2003). https://doi.org/10.1083/jcb.200303020

38 Finlay-Schultz, J. *et al.* New generation breast cancer cell lines developed from patient-derived xenografts. *Breast Cancer Res* **22**, 68 (2020). https://doi.org/10.1186/s13058-020-01300-y

39 Finlay-Schultz, J. *et al.* Breast Cancer Suppression by Progesterone Receptors Is Mediated by Their Modulation of Estrogen Receptors and RNA Polymerase III. *Cancer Res* **77**, 4934-4946 (2017). https://doi.org/10.1158/0008-5472.CAN-16-3541

40 Aonurm-Helm, A., Berezin, V., Bock, E. & Zharkovsky, A. NCAM-mimetic, FGL peptide, restores disrupted fibroblast growth factor receptor (FGFR) phosphorylation and FGFR mediated signaling in neural cell adhesion molecule (NCAM)-deficient mice. *Brain Res* **1309**, 1-8 (2010). https://doi.org/10.1016/j.brainres.2009.11.003

41 Francavilla, C. *et al.* The binding of NCAM to FGFR1 induces a specific cellular response mediated by receptor trafficking. *J Cell Biol* **187**, 1101-1116 (2009). https://doi.org/10.1083/jcb.200903030

42 Niethammer, P. *et al.* Cosignaling of NCAM via lipid rafts and the FGF receptor is required for neuritogenesis. *J Cell Biol* **157**, 521-532 (2002). https://doi.org/10.1083/jcb.200109059
43 Zeng, Q. *et al.* Synaptic proximity enables NMDAR signalling to promote brain metastasis. *Nature* **573**, 526-531 (2019). https://doi.org/10.1038/s41586-019-1576-6
44 Venkataramani, V. *et al.* Direct excitatory synapses between neurons and tumor cells drive brain metastatic seeding of breast cancer and melanoma. *bioRxiv*, 2024.2001.2008.574608 (2024). https://doi.org/10.1101/2024.01.08.574608
45 Savchuk, S. *et al.* Neuronal-Activity Dependent Mechanisms of Small Cell Lung Cancer Progression. *bioRxiv* (2023). https://doi.org/10.1101/2023.01.19.524430
46 Bado, I. L. *et al.* The bone microenvironment increases phenotypic plasticity of ER(+) breast cancer cells. *Dev Cell* **56**, 1100-1117 e1109 (2021). https://doi.org/10.1016/j.devcel.2021.03.008
47 Chadashvili, T. & Peterson, D. A. Cytoarchitecture of fibroblast growth factor receptor 2 (FGFR-2) immunoreactivity in astrocytes of neurogenic and non-neurogenic regions of the young adult and aged rat brain. *J Comp Neurol* **498**, 1-15 (2006). https://doi.org/10.1002/cne.21009
48 Huang, C., Yuan, P., Wu, J. & Huang, J. Estrogen regulates excitatory amino acid carrier 1 (EAAC1) expression through sphingosine kinase 1 (SphK1) transacting FGFR-mediated ERK signaling in rat C6 astroglial cells. *Neuroscience* **319**, 9-22 (2016). https://doi.org/10.1016/j.neuroscience.2016.01.027
49 Jurgenson, M., Aonurm-Helm, A. & Zharkovsky, A. Partial reduction in neural cell adhesion molecule (NCAM) in heterozygous mice induces depression-related behaviour without cognitive impairment. *Brain Res* **1447**, 106-118 (2012). https://doi.org/10.1016/j.brainres.2012.01.056
50 Francavilla, C. *et al.* Neural cell adhesion molecule regulates the cellular response to fibroblast growth factor. *J Cell Sci* **120**, 4388-4394 (2007). https://doi.org/10.1242/jcs.010744
51 Venkatesh, H. S. *et al.* Electrical and synaptic integration of glioma into neural circuits. *Nature* **573**, 539-545 (2019). https://doi.org/10.1038/s41586-019-1563-y
52 Venkataramani, V. *et al.* Glutamatergic synaptic input to glioma cells drives brain tumour progression. *Nature* **573**, 532-538 (2019). https://doi.org/10.1038/s41586-019-1564-x
53 Knight, W. *et al.* Abstract 6296: Preclinical evaluation of a panel of FGFR inhibitors for their normal brain and brain tumor distribution. *Cancer Research* **82**, 6296-6296 (2022). https://doi.org/10.1158/1538-7445.Am2022-6296
54 Coombes, R. C. *et al.* Results of the phase IIa RADICAL trial of the FGFR inhibitor AZD4547 in endocrine resistant breast cancer. *Nat Commun* **13**, 3246 (2022). https://doi.org/10.1038/s41467-022-30666-0
55 Zhang, C., Lowery, F. J. & Yu, D. Intracarotid Cancer Cell Injection to Produce Mouse Models of Brain Metastasis. *J Vis Exp* (2017). https://doi.org/10.3791/55085
56 Zhang, C. & Yu, D. Microenvironment determinants of brain metastasis. *Cell Biosci* **1**, 8 (2011). https://doi.org/10.1186/2045-3701-1-8
57 Miarka, L. & Valiente, M. Animal models of brain metastasis. *Neurooncol Adv* **3**, v144-v156 (2021). https://doi.org/10.1093/noajnl/vdab115
58 Koza, L. A. *et al.* Immunocal(R) limits gliosis in mouse models of repetitive mild-moderate traumatic brain injury. *Brain Res* **1808**, 148338 (2023). https://doi.org/10.1016/j.brainres.2023.148338
59 Pierce, A. M. *et al.* Establishment of patient-derived orthotopic xenograft model of 1q+ posterior fossa group A ependymoma. *Neuro Oncol* **21**, 1540-1551 (2019). https://doi.org/10.1093/neuonc/noz116
60 de Vellis, J. & Cole, R. Preparation of mixed glial cultures from postnatal rat brain. *Methods Mol Biol* **814**, 49-59 (2012). https://doi.org/10.1007/978-1-61779-452-0_4
61 Pertusa, M., Garcia-Matas, S., Rodriguez-Farre, E., Sanfeliu, C. & Cristofol, R. Astrocytes aged in vitro show a decreased neuroprotective capacity. *J Neurochem* **101**, 794-805 (2007). https://doi.org/10.1111/j.1471-4159.2006.04369.x
62 NanoStringNCTools: NanoString nCounter Tools (2024).
63 GeomxTools: NanoString GeoMx Tools (2024).
64 GeoMxWorkflows: GeoMx Digital Spatial Profiler (DSP) data analysis workflows (2024).
65 Liu, N. *et al.* standR: spatial transcriptomic analysis for GeoMx DSP data. *Nucleic Acids Res* **52**, e2 (2024). https://doi.org/10.1093/nar/gkad1026
66 Ritchie, M. E. *et al.* limma powers differential expression analyses for RNA-sequencing and microarray studies. *Nucleic Acids Res* **43**, e47 (2015). https://doi.org/10.1093/nar/gkv007

67 GeoMXAnalysisWorkflow: GeoMXAnalysisWorkflow (2023).
68 msigdb: An ExperimentHub Package for the Molecular Signatures Database (MSigDB) (2024).
69 GSEABase: Gene set enrichment data structures and methods (2024).
70 vissE: Visualising Set Enrichment Analysis Results (2024).
71 igraph: Network Analysis and Visualization in R (2025).
72 Love, M. I., Huber, W. & Anders, S. Moderated estimation of fold change and dispersion for RNA-seq data with DESeq2. *Genome Biol* **15**, 550 (2014). https://doi.org/10.1186/s13059-014-0550-8
73 Beaudoin, G. M., 3rd *et al.* Culturing pyramidal neurons from the early postnatal mouse hippocampus and cortex. *Nat Protoc* **7**, 1741-1754 (2012). https://doi.org/10.1038/nprot.2012.099
74 Wang, Y. *et al.* SynQuant: an automatic tool to quantify synapses from microscopy images. *Bioinformatics* **36**, 1599-1606 (2020). https://doi.org/10.1093/bioinformatics/btz760
75 "The image stabilizer plugin for ImageJ," https://www.cs.cmu.edu/~kangli/code/Image_Stabilizer.html (2008).
76 Tinevez, J. Y. *et al.* TrackMate: An open and extensible platform for single-particle tracking. *Methods* **115**, 80-90 (2017). https://doi.org/10.1016/j.ymeth.2016.09.016
77 Ershov, D. *et al.* TrackMate 7: integrating state-of-the-art segmentation algorithms into tracking pipelines. *Nat Methods* **19**, 829-832 (2022). https://doi.org/10.1038/s41592-022-01507-1
78 Zhang, Y. *et al.* Purification and Characterization of Progenitor and Mature Human Astrocytes Reveals Transcriptional and Functional Differences with Mouse. *Neuron* **89**, 37-53 (2016). https://doi.org/10.1016/j.neuron.2015.11.013
79 Clarke, L. E. *et al.* Normal aging induces A1-like astrocyte reactivity. *Proc Natl Acad Sci U S A* **115**, E1896-E1905 (2018). https://doi.org/10.1073/pnas.1800165115